Mineralogical Magazine (2021), **85**, 496–513
doi:10.1180/mgm.2021.56

CAMBRIDGE UNIVERSITY PRESS

Article – Gregory Yu. Ivanyuk memorial issue

Burbankite and pseudomorphs from the Main Intrusion calcite carbonatite, Lofdal, Namibia: association, mineral composition, Raman spectroscopy

Maria A. Sitnikova[1]*, Vicky Do Cabo[2], Frances Wall[3] and Simon Goldmann[1]

[1]Federal Institute for Geosciences and Mineral Resources (BGR), Stilleweg, 2, 30655 Hannover, Germany; [2]Geological Survey of Namibia, 6 Aviation Road Private Bag 13297 Windhoek, Namibia; and [3]Camborne School of Mines, University of Exeter, Cornwall TR10 9FE, UK

Abstract

The Neoproterozoic Lofdal alkaline carbonatite complex consists of a swarm of carbonatite dykes and two plugs of calcite carbonatite known as the 'Main' and 'Emanya' carbonatite intrusions, with associated dykes and plugs of phonolite, syenite, rare gabbro, anorthosite and quartz-feldspar porphyry. In the unaltered Main Intrusion calcite carbonatite the principal rare-earth host is burbankite. As burbankite typically forms in a magmatic environment, close to the carbohydrothermal transition, this has considerable petrogenetic significance. Compositional and textural features of Lofdal calcite carbonatites indicate that burbankite formed syngenetically with the host calcite at the magmatic stage of carbonatite evolution. The early crystallisation of burbankite provides evidence that the carbonatitic magma was enriched in Na, Sr, Ba and light rare earth elements. In common with other carbonatites, the Lofdal burbankite was variably affected by alteration to produce a complex secondary mineral assemblage. Different stages of burbankite alteration are observed, from completely fresh blebs and hexagonal crystals through to complete pseudomorphs, consisting of carbocernaite, ancylite, cordylite, strontianite, celestine, parisite and baryte. Although most research and exploration at Lofdal has focused on xenotime-bearing carbonatite dykes and wall-rock alteration, this complex also contains a more typical calcite carbonatite enriched in light rare earth elements and their alteration products.

Keywords: Lofdal, Namibia, carbonatites, burbankite, carbocernaite, cordylite, pseudomorphs

(Received 23 September 2020; accepted 28 May 2021; Accepted Manuscript published online: 1 July 2021; Guest Associate Editor: Anton R. Chakhmouradian)

Introduction

One of the key genetic questions about the magmas that produce carbonatites is their original enrichment in alkalis. This has been a subject of scientific debate for more than 30 years (Kapustin, 1983; Keller, 1989; Gittins, 1989; Le Bas, 1989, 2008; Dawson, 2008; Guzmics *et al.*, 2011, 2015, 2019; Keller and Zaitsev, 2012; Zaitsev *et al.*, 2013; Elliott *et al.*, 2018). The occurrence of alkali carbonates and alkali-bearing silicates in primary (magmatic) carbonatites provides insight into the role of alkalis in the petrological evolution of these rocks.

Many carbonatites show evidence of extensive hydrothermal reworking and the Lofdal carbonatites are not an exception. During recent years, most interest has been focused on the xenotime-bearing Lofdal carbonatite dykes and fenites as an unusual potential source for heavy rare earth elements (Wall *et al.*, 2008; Namibia Rare Earths Inc. Reports, 2011–2014; Swinden and Siegfried, 2012; Williams-Jones *et al.*, 2015; Bodeving *et al.*, 2017). At Lofdal, there is limited information about the largest carbonatite intrusion, the Main Intrusion because it is homogeneous, has a lower rare earth element (REE) content and is characterised by a typical pattern of enrichment in light REE (LREE = La–Nd) compared to carbonatite dykes and Lofdal Area 4, which are enriched in heavy REE (Swinden and Siegfried, 2012; Namibia Rare Earth Inc's report, 2012). In this contribution, we focus on the Main Intrusion to describe and interpret this carbonatite and its REE mineralogy.

The primary rare earth mineral in the calcite carbonatite intrusion is burbankite, a mineral of petrogenetic significance. This typically forms in a magmatic environment or close to the magmatic–hydrothermal transition – carbohydrothermal stage (Zaitsev *et al.*, 1996, 1998), although is readily altered, typically leaving pseudomorphs. Burbankite and/or its pseudomorphs have been reported from a number of other carbonatites worldwide (Borodin and Kapustin, 1962; Zdorik, 1966; Wall and Mariano, 1996; Zaitsev *et al.*, 1997, 1998, 2002; Subbotin *et al.*, 1999; Wall and Zaitsev, 2004; Moore *et al.*, 2015; Chakhmouradian *et al.*, 2017). Here we report new data on burbankite paragenesis, composition and Raman spectroscopy from the Main Intrusion and one calcite carbonatite dyke at Lofdal.

***Author for correspondence:** Maria A. Sitnikova, Email: maria.sitnikova@bgr.de
This paper is part of a thematic set 'Alkaline Rocks' in memory of Dr. Gregory Yu. Ivanyuk
Cite this article: Sitnikova M.A., Do Cabo V., Wall F. and Goldmann S. (2021) Burbankite and pseudomorphs from the Main Intrusion calcite carbonatite, Lofdal, Namibia: association, mineral composition, Raman spectroscopy. *Mineralogical Magazine* **85**, 496–513. https://doi.org/10.1180/mgm.2021.56

Materials and methods

Whole-rock geochemistry

Whole-rock geochemical analyses were obtained for six samples to characterise the bulk composition of the calcite carbonatites of the Main Intrusion, the Emanya plug and the coarse-grained calcite carbonatite dyke. The analyses were undertaken at the Federal Institute for Geosciences and Natural Resorces (Bundesanstaldt für Gowissenschaften und Rohstoffe – BGR), Hannover, Germany, analytical laboratory and performed by X-ray fluorescence analysis and inductively coupled plasma mass spectrometry (ICP-MS) techniques. Major- and trace-element concentrations were measured by wavelength-dispersive X-ray fluorescence analysis (WDX) on powdered bulk samples using a Panalytical Axios spectrometer (Panalytical, Almelo, Netherlands). Sample preparation included mixing a pulverised sample with lithium metaborate (Spectroflux, Flux 162 No. 100A, Alfa Aesar) as flux material and melting the mixture into glass beads. The loss on ignition (LOI) was analysed by heating 1 g of sample to 1030°C for 10 minutes. For ICP-MS analysis, ~100 mg of powdered sample was dissolved with 0.5 ml HNO_3 plus 2 ml HF. After dissolution, the solutions were evaporated to dryness, then dissolved in HNO_3 and aliquots corresponding to 4 mg of sample prepared for ICP-MS measurement. Element concentrations were determined using an Agilent 7500ce instrument equipped with an autosampler (for details, see Estrada *et al.*, 2012).

Microanalytical methods

Six polished thin sections from Lofdal alkaline carbonatite complex carbonatites were investigated by scanning electron microscope (SEM). Microanalysis on the thin sections was performed using a ZEISS SIGMA 300VP SEM, equipped with a back-scattered electron (BSE) detector and two Bruker XFlash 6|30 energy-dispersive X-ray spectroscopy (EDS) detectors, with 129 eV energy resolution and the ZEISS *Mineralogic* automated quantitative mineralogy software platform located at BGR, Hannover, Germany. Within each thin section, several areas of interest were selected and imaged to provide a high-resolution mosaic of stitched BSE images. Additionally a quantitative mineralogical analysis was carried out on this region of interest, using *Mineralogic* software, creating a mineral map with a defined step size as well as a list with parameters for grains in the sample. The acceleration voltage of the primary electron beam was set to 25 kV, to ensure X-ray excitation for all relevant elements (e.g. REE, Sr, Ba). The 120 µm aperture was used to obtain a high input count rate for the EDS detectors, dwell time was 0.01 s, with 10 µm mapping step size and 90x magnification, the montage image consists of 293 single fields. The EDS software is fully integrated with the *Mineralogic* software. A detailed description of the *Mineralogic* method is given in Graham and Keulen (2019) and Keulen *et al.* (2020).

Raman spectroscopy

The investigation of burbankite, carbocernaite, cordylite and ancylite was performed using a Renishaw inVia Qontor confocal micro-Raman system equipped with a Leica DM 2700 microscope with an N plan 100× objective lens with 0.85 numerical aperture, which was used to focus the laser beam and collect scattered radiation from the sample. A continuous wave HeNe laser with a wavelength of 633 nm was used as the excitation source. Unpolarised spectra were recorded by a Renishaw Centrus 1873H8 detector with a charge coupled device (CCD) array of 1040 × 256 pixels using an 1800 lines/mm grating. The spectral resolutions was estimated to be better than 1 cm^{-1}. The instrument was calibrated by automatic alignment procedures of the software *WiRE* including laser spot correction, CCD area, and slit alignments. The correctness of the calibration was verified with 520.5 cm^{-1} band of an unprocessed (111) mirror-polished Si standard. All spectra were acquired with an integration time of 20 s and a laser power of 20 mW. Raw spectra were processed by the *WiRE* software. Thereby, background was subtracted and spikes caused by cosmic ray events were filtered out. The spectral range of the measurements was truncated to an area from 0 to 1300 cm^{-1}, which is relevant to carbonate spectra. The benefit of the spectral reduction is an improved curve fit procedure that avoids high fluorescence spectra from epoxy resin towards higher wavenumbers. Position, intensity and full width at half maximum of the Raman bands were determined using the curve fit function of the software.

SEM with integrated Raman system

The various carbonates and sulfates are indistinguishable when viewed in reflected light mode with the Raman instrument (see description above). To identify the individual constituents of burbankite pseudomorphs, a new technique of combining SEM and BSE imaging with Raman spectroscopy was used. An area of interest was chosen within a BSE image and then specific points within that area were analysed by Raman spectroscopy. The Raman spectra were acquired with a correlative confocal Raman and scanning electron microscope (Sigma 300 RISE) equipped with a piezo scan stage (Wille *et al.*, 2018; Schmidt *et al.*, 2019). The excitation light source was a linear polarised (0°) coherent compass sapphire laser with 532 nm wavelength (WITec, Ulm, Germany) focused through a 100× (NA = 0.75) vacuum objective (Carl Zeiss, Jena, Germany). The laser beam was focused onto the sample surface and generated a Raman signal with spatial resolution of ~ 1 µm. The Raman-scattering signal was collected by the same objective, and detected by an UHTS 300 spectrograph equipped with a diffraction grating of 1200 grooves/mm. The spectral resolution of the instrument is 1 cm^{-1}. The spectrometer was calibrated using a synthetic Si standard. All spectra were acquired with an integration time of 20 s and a laser power of 20 mW. The control *FIVE* (WITec) acquisition software was used to set experimental parameters for hyperspectral image acquisition and for spectral processing.

Reference spectra of well-characterised samples of burbankite, carbocernaite, parisite, bastnäsite and cordylite from the BGR mineral collection were acquired with the same instrument and stored in the Raman spectra database. Sodium in REE carbonates such as burbankite, carbocernaite, ancylite and cordylite, is challenging to analyse accurately by WDS analysis. EDS is better for analysing sodium, though with this technique it is not trivial to make precise analyses of the minor components (Chakhmouradian *et al.*, 2017). Therefore we checked every grain analysed with the electron microprobe by laser-Raman so that any contaminated compositions can be excluded. The SEM with integrated Raman technique was used as an additional 'express-method' for mineral identification.

Electron probe microanalysis (EPMA)

Prior to EPMA, back-scattered electron imaging was used to check the homogeneity of the crystals and locate suitable areas

https://doi.org/10.1180/mgm.2021.56 Published online by Cambridge University Press

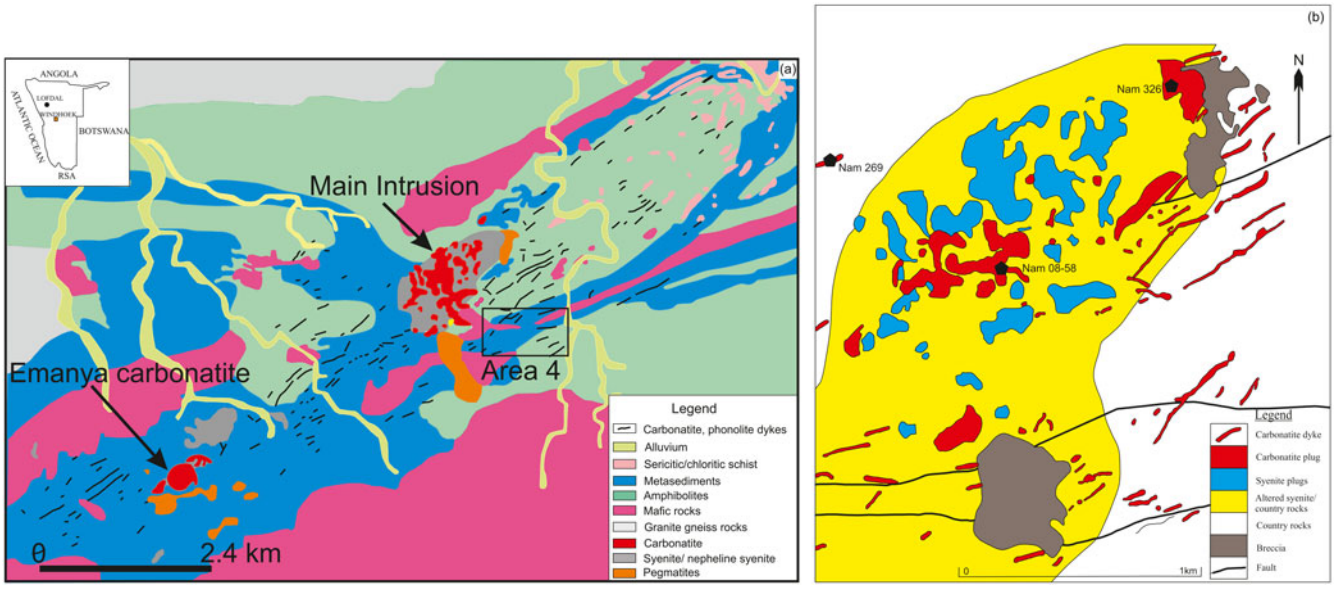

Fig. 1. (a) Simplified geological map of the Lofdal area after unpublished maps of Namibia Rare Earths (Pty) Ltd. and Do Cabo (2014). Insert shows location of the Lofdal Intrusive Suite. (b) Simplified geological map of the Main Intrusion after unpublished maps of Namibia Rare Earths (Pty) Ltd. and DoCabo (2014).

for analysis. The composition of selected minerals was determined on carbon-coated polished thin sections by wavelength-dispersive X-ray spectrometry using CAMECA SX-100 and JEOL JXA-8530F electron microprobes at BGR, Hannover, Germany. The operational settings including acceleration voltage, probe current and other specific parameters (spectral lines, detector crystals, standards and peak counting times) are summarised in the Supplementary material. Relatively low accelerating voltages and probe currents were applied in order to reduce the crystal damage under the electron beam. Additionally, the electron beam was defocused to 10 µm in order to minimise crystal damage and volatility of Na, K and F. Therefore, these elements were quantified prior to the rest of the elements to minimise the effect of volatility. A much larger beam diameter is suggested for REE carbonates, e.g. 20 µm for burbankite (A.N. Zaitsev, personal communication), however this was not realistic in our case because of the small size of the minerals analysed. All elements were calibrated against natural minerals, synthetic materials and pure metals as primary standards (see Supplementary material). Peak interferences were identified on standards measured as unknowns and correction factors were obtained for empirical interference corrections. Detection limits for each element are given for each mineral phase in the respective table of analytical results.

Regardless of all these precautions, uncertainties cannot be avoided during EPMA of carbonates resulting from the inability to measure CO_2, the relatively small beam diameter, volatility of alkalis, and high interference corrections (c.f. Zaitsev, 1998; Chakhmouradian and Dahlgren, 2021). A detailed description of probe settings can be found in the Supplementary material (see below).

Geology of Lofdal carbonatites

The Lofdal alkaline-carbonatite complex is located 20°21′00″S and 14°45′20″E on the Bergville and Lofdal farms northwest of Khorixas in Damaraland, in the Kunene Region of the Republic of Namibia (Fig. 1). It consists of a swarm of dykes, mainly calcite carbonatite, together with dolomite and ankerite carbonatite dykes and two plugs of calcite carbonatite known as 'Main' and 'Emanya' carbonatite intrusions. The complex also has many phonolite dykes, plugs of nepheline syenite and syenite and rare mafic rocks. These all intrude into the Huab Metamorphic Complex basement within a NE–SW shear zone over 30 km long. The Lofdal alkaline-carbonatite complex is Neoproterozoic, with a radiometric age of 765 Ma (Wall *et al.*, 2008; Do Cabo, 2014), which is pre-orogenic and related to an intra-continental rift environment (Miller, 2008). Geological and geochemistry reviews of the Lofdal alkaline-carbonatite complex can be found in the literature (Wall *et al.*, 2008; Do Cabo, 2014, Namibia Rare Earths Inc. reports, Bodeving *et al.*, 2017).

The largest carbonatite intrusion in the Lofdal complex is the calcite carbonatite Main Intrusion (Fig. 1b). This occupies ~4 km^2, trends NNW–SSE and intrudes nepheline syenite, forming patches of coarse-grained white calcite carbonatite. Syenitic rocks and coarse polymictic breccias are associated closely with the calcite carbonatite plug. In places the nepheline syenite and carbonatite contacts are sharp with an observed zone of alteration up to tens of metres into the syenites. The other sizable intrusion is the Emanya calcite carbonatite, and although this has been analysed here for comparison of whole-rock composition, the appearance of Emanya, which consists of a dark brown fine-grained mixture of iron oxides with calcite, is an extensively altered, oxidised carbonatite in contrast with the Main Intrusion. Its mineralogy is distinct and neither burbankite nor its pseudomorphs have been found to occur. Hence, these rocks are not described in detail here.

The majority of the phonolite and carbonatite dykes range from a few centimetres to 30 m in width and extend up to 15 km along strike. They crosscut, interfinger, run in parallel with one another, and in places thin out completely, and/or crosscut other intrusions, mainly the syenites, granites and earlier phonolites. Some dykes are composite, with multiple intrusions of earlier granitic pegmatite, phonolite and carbonatite. In contrast

https://doi.org/10.1180/mgm.2021.56 Published online by Cambridge University Press

Table 1. Representative whole-rock major- and trace-element compositions of calcite carbonatites from the Lofdal.

Rock type	Main Intrusion	'zero' dyke	Main Intrusion	Emanya plug	Dykes of Area 4			
Sample	08_058	269	326	949	881G	881R	189	927
Wt.%								
SiO_2	2.57	1.72	0.18	2.24	2.13	1.13	2.54	2.92
TiO_2	0.01	0.26	<0.001	0.33	0.39	0.07	0.02	0.18
Al_2O_3	0.47	0.51	<0.05	0.45	<0.05	0.31	0.38	0.54
Fe_2O_3	1.48	9.51	1.35	16.16	2.53	20.96	25.40	11.81
MnO	0.41	2.74	1.10	2.59	1.59	2.45	0.79	0.92
MgO	0.08	0.71	0.13	5.14	0.29	0.72	1.64	1.70
CaO	50.87	43.41	52.91	36.45	51.33	40.60	34.50	42.32
Na_2O	0.21	0.08	<0.01	<0.01	<0.01	<0.01	0.09	0.02
K_2O	0.22	0.09	<0.005	0.25	0.01	0.09	0.01	0.26
P_2O_5	0.11	1.23	0.04	0.02	0.17	0.03	2.60	1.56
SO_3	0.21	0.28	0.01	0.04	0.02	0.06	0.12	0.08
Cl	0.01	0.01	0.02	0.00	0.01	0.01	0.01	0.01
F	0.08	1.08	0.08	0.15	0.28	<0.05	0.10	0.23
LOI	41.00	34.85	42.63	35.26	40.87	33.29	30.46	35.08
–O = F,Cl	0.03	0.45	0.03	0.06	0.12	-	0.04	0.10
Total	97.70	96.02	98.41	99.00	99.53	99.69	98.59	97.53
Element, ppm								
As	<2*	43	<2	13	8	8	162	23
Ba	717	4472	290	24	132	48	169	396
Bi	<3	20	<3	<3	4	4	4	<3
Co	<3	8	<3	12	6	28	86	68
Cr	<5	<5	<5	<5	<5	<5	64	25
Cs	<4	<4	<4	8	<4	<4	<4	<4
Cu	28	22	19	25	34	52	<4	<4
Ga	2	3	<2	<2	<2	<2	<2	<2
Hf	<7	<8	<7	<8	<7	<8	<9	22
Mo	<3	46	<3	21	<3	10	29	17
Nb	78	166	8	135	185	38	20	266
Ni	<3	<3	<3	8	<3	6	28	17
Pb	7	64	8	6	9	<4	68	171
Rb	12	15	6	18	9	14	13	28
Sb	<12	<12	<12	<11	<12	<11	<11	<12
Sc	<3	5	<3	6	6	8	70	42
Sn	<5	<5	<5	5	<5	<5	<5	<5
Sr	16,810	18,640	11,490	427	1465	457	744	638
Ta	<5	<6	<5	<6	<5	<6	<7	<6
Th	40	190	30	80	51	19	1521	7424
U	<5	<5	<5	7	6	6	19	189
W	7	31	<7	20	n.d.	n.d.	239	228
V	<4	37	<5	19	44	40	187	90
Zn	11	864	9	31	16	65	83	92
Zr	85	352	33	12	14	13	198	3602
La	238	2032	265	2089	228	141	190	68
Ce	442	3488	512	3312	357	234	341	198
Pr	45	351	53	299	34	25	38	30
Nd	150	1133	172	892	104	79	158	152
Sm	22	143	23	79	17	11	227	128
Eu	6	38	6	19	6	4	102	71
Gd	16	103	18	43	18	9	291	286
Tb	2	16	3	5	3	1	41	60
Dy	13	107	15	27	24	10	180	353
Y	60	642	72	130	129	50	584	1835
Ho	2	24	3	5	5	2	26	66
Er	6	72	9	17	19	8	57	175
Tm	1	11	1	3	4	2	7	25
Yb	5	70	8	22	29	15	38	161
Lu	1	10	1	3	5	3	5	23
Element ratios								
LREE	875	7004	1002	6592	724	478	727	448
MREE	45	284	47	140	41	24	620	485
HREE	90	951	111	212	219	91	937	2698
ΣREE	1010	8239	1160	6944	983	593	2284	3631
La/Lu	355	213	219	604	49	53	41	3
$(La/Yb)_n$	32	20	22	67	5	7	3	0

*Detection limit, for example < 2 indicates measurement was below detection limit (d.l.) of 2 ppm.

https://doi.org/10.1180/mgm.2021.56 Published online by Cambridge University Press

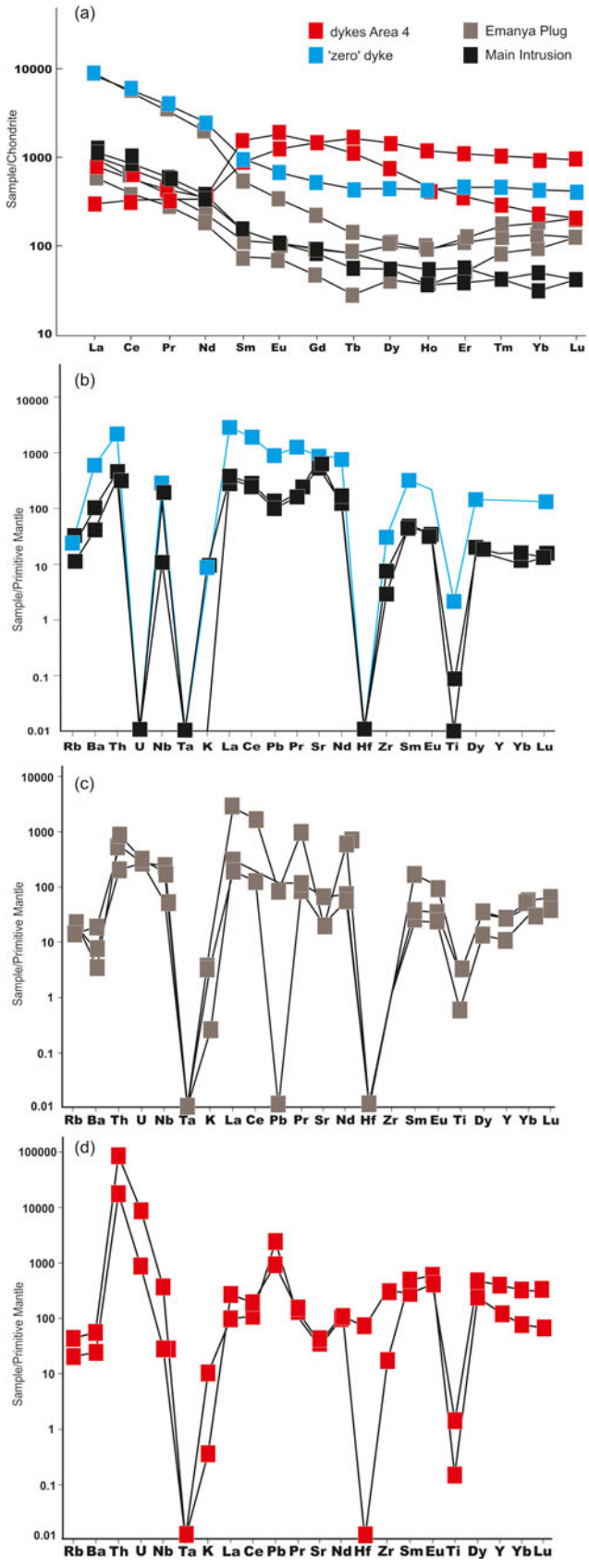

Fig. 2. (a) Chondrite-normalised REE distribution patterns of carbonatites from the Main and Emanya Intrusions. (b–d) Primitive mantle-normalised trace-element distribution patterns of (b) the Main Intrusion carbonatite and 'zero' carbonatite dyke; (c) Emanya plug; (d) Carbonatite dykes of Area 4. The primitive mantle values are from Sun and McDonough (1989).

to the coarse-grained white calcite carbonatite dyke investigated, most of the Lofdal carbonatite dykes appear with shades of brown, banding and evidence of sub-solidus alteration. Some of them are so extensively altered that they have been interpreted as hydrothermal veins rather than dykes (Williams-Jones *et al.*, 2015). The dyke sample analysed here (Nam-269) is distinct from the xenotime-bearing dykes of Area 4 and consists of white calcite and is more like the Main Intrusion calcite carbonatite. It is situated close to the Main Intrusion (Fig. 1b). Do Cabo (2014) named these kind of dykes, the 'zero' dykes because of their affinity to the Main Intrusion.

Geochemistry of Lofdal calcite carbonatites

Two samples from the Main calcite carbonatite plug, namely sample 08-58, 326 and sample 269 from the 'zero' dyke of unaltered calcite carbonatite were analysed for major and trace elements (Table 1). For comparison we also include our geochemical data on the Emanya carbonatite plug (sample 881R, 881G, 949) and on the dykes of Area 4 (samples 927 and 189).

The carbonatites of the Main Intrusion are classified as calcite carbonatite ($CaO/(CaO + MnO + FeO + MgO)$ ≈0.99 on average). Their FeO content ranges from 1.3 to 9.5 wt.% and their MgO content averages 0.3 wt.%. Significant variation in FeO, Na_2O, SiO_2 and P_2O_5, Ba, Sr and Nb (Table 1) results from the variable modal contents of magnetite, aegirine–augite, apatite, phlogopite, pyrochlore and REE-Sr-Ba-carbonates which is, at least in part, due to magmatic flow segregation. The chondrite-normalised REE distribution patterns of the Main Intrusion, Emanya plug and 'zero' dyke (Fig. 2a) are characterised by strong LREE enrichment and absence of Eu anomaly. For comparison we provide also patterns for carbonatite dykes of Area 4 which show elevated levels of heavy lanthanides (Fig. 2a).

Compared to the alkaline silicate rocks at Lofdal (figure 3 in Bodeving *et al.*, 2017, p.389), the carbonatites are depleted in Ta, Pb, Zr and Hf and enriched in Sr and the light REE (Fig. 2b–d). A distinctive geochemical characteristic of the Main Intrusion calcite carbonatites is the relatively low (for Lofdal) average ΣREE concentration 0.1 wt.% (Table 1), and low LREE/HREE ratios of $(La/Yb)_n$ of 22–32 compared to all carbonatites worldwide (Woolley and Kempe, 1989). This carbonatite also has the lowest concentrations of other trace elements compared with the other Lofdal carbonatite groups, particularly the high-field-strength elements: Th, U, Nb, Hf and Zr (Fig. 2b–d) and in Do Cabo, (2014). The SrO content ranges between 1.1 to 1.8 wt.%, which represents the highest values at Lofdal.

One of the calcite carbonatite bodies in the dyke swarm (269 – 'zero' dyke) exhibits a geochemical pattern very similar to that of the carbonatite of the Main Intrusion (Table 1, Fig. 2a,b). The ΣREE concentration of 0.8 wt.% (Table 1) is slightly higher compared to the Main Intrusion although the $(La/Yb)_n$ ratio of 20 is similar to that of the Main Intrusion. The 'zero' dyke has higher Ba, Th, Nb, Y, Zn, Zr and Sr concentrations than the Main Intrusion carbonatite.

The Emanya calcite carbonatite is richer in LREE compared with the Main Intrusion carbonatite (Table 1, Fig. 2), although this still has LREE average, minimum and maximum contents within the global values for calcite carbonatite (Woolley and Kempe, 1989). The $(La/Yb)_n$ ratios range from 5 to 67. The normalised REE distribution patterns between Tb to Lu exhibit a slightly positive slope compared to those of the Main Intrusion. The different character of the REE distribution is possibly a

https://doi.org/10.1180/mgm.2021.56 Published online by Cambridge University Press

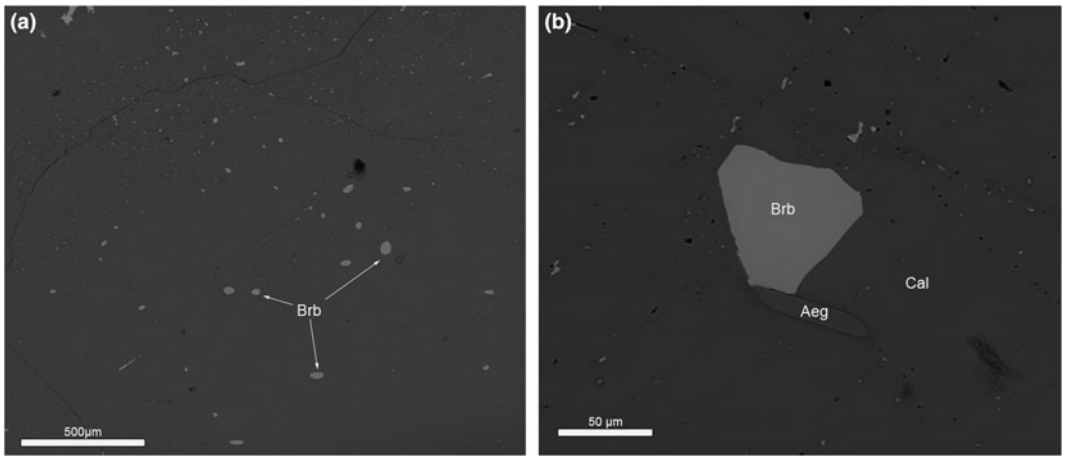

Fig. 3. (a) Ovoid primary burbankite (Brb) inclusion in calcite. (b) Hexagonal crystal of burbankite in primary calcite (Cal). Aeg – aegirine. BSE images.

consequencet of the extensive sub-solidus alteration of the Emanya carbonatite. Emanya has the lowest whole-rock Th contents at Lofdal, between 19 and 80 ppm (av. 50 ppm). The Nb concentration is variable, ranging between 38 and 185 ppm, compared with a Lofdal average value of 112 ppm Nb (Do Cabo, 2014).

The xenotime-bearing dykes of Area 4 (samples 189 and 927) are represented by intensively sheared and altered carbonatites with high iron contents and levels of oxidation. These rocks are enriched in the middle REE and high REE (MREE and HREE, respectively), and the dyke REE distribution patterns are characterised by high HREE/LREE ratios (Fig. 2a). The most important characteristic of the rocks is their extremely low LREE concentrations, which are lower than the concentrations in the Main Intrusion although similar to Emanya carbonatites.

In contrast, the concentrations of MREE and HREE exceed the averages for carbonatites, as seen in xenotime-bearing dykes elsewhere at Lofdal (Wall *et al.*, 2008). The xenotime-bearing dykes have the highest contents of Hf, Th, U and Zr at Lofdal.

Burbankite paragenesis

The burbankite group consists of six mineral species with the general formula $A_3B_3(CO_3)_5$ where A = Na > Ca, REE^{3+}, □ (vacancy); B = Sr, Ca, Ba, REE^{3+}, Na giving: burbankite $(Na,Ca,□)_3(Sr,REE,Ba,Ca)_3(CO_3)_5$, khanneshite $(Na,Ca)_3(Ba,Sr,REE,Ca)_3(CO_3)_5$, calcioburbankite $(Na,Ca,REE)_3(Ca,REE,Sr)_3(CO_3)_5$, remondite-(Ce) $Na_3(Ce,Ca,Na,Sr)_3(CO_3)_5$, remondite-(La) $Na_3(La,Ce,Ca)_3(CO_3)_5$ and petersenite-(Ce) $(Na,Ca)_4(Ce,La,Sr)_2(CO_3)_5$. Burbankite is the most common mineral; other members of the group are rare.

Burbankite was observed in all six samples of the Main Intrusion calcite carbonatite and the 'zero' calcite carbonatite dyke at Lofdal alkaline-carbonatite complex. In the Main Intrusion it occurs as small ovoid inclusions (Fig. 3a) or small hexagonal crystals (Fig. 3b) in the core of primary calcite crystals. The burbankite inclusions in coarse-grained primary calcite carbonatite vary from 10 to 100 µm in size (Fig. 3a,b). The calcite crystals (grain size 0.1–0.5 mm) are characterised by polysynthetic twins (Fig. 4a), sharp grain boundaries with no resorption traces and are enriched in Sr (0.8–2.1 wt.% SrO – Table 2). The proportion of burbankite in calcite carbonatite of the Main Intrusion varies from sample to sample from 0.5 to 1 volume percent according to results of automated mineralogical analysis (see Microanalytical methods).

Locally, some areas of primary calcite have undergone fluid interaction resulting in resorption of the calcite grain boundaries and formation of numerous tiny strontianite inclusions in the outer parts of the calcite crystals, along the grain boundaries and cleavage planes (Fig. 4b). Similar strontianite inclusions, dispersed throughout the peripheral parts of calcite crystals and along cleavage planes, were observed in calcite carbonatite at Fen, Norway (Chakhmouradian and Dahlgren, 2021), and interpreted as a product of calcite interaction with fluids (Chakhmouradian *et al.*, 2016). The composition of calcite at Lofdal changes from high-Sr (bright areas under BSE) in the central parts to low Sr (dark areas under BSE) along the grain boundaries and cleavage planes (Fig. 4c, Table 2). In this mineral association, alteration of burbankite was observed (Fig. 4d) with the crystals being resorbed and replaced by carbocernaite and bastnäsite. Small dissolution cavities and veinlets in calcite carbonatite are commonly filled with an association of the following minerals: strontianite; calcite; carbocernaite; bastnäsite; parisite; baryte; celestine; and rarely with ancylite and monazite (Fig. 4f,g). Cavities are typically filled with quartz (Fig. 4e). The identification of these minerals was made using Raman spectroscopy, EDS and WDS analysis (Tables 3, 4, 5).

Calcite carbonatite of the Main Intrusion close to the contact zone with nepheline syenites is enriched in aegirine–augite, K-feldspar, fluorapatite, albite and fluorite (Fig. 5). Along grain boundaries and cleavage planes the calcite in this association has undergone some chemical alteration and has lost Sr (Table 2, an. 3, 4). Aegirine–augite and K-feldspar occur as poikilitic crystals with numerous calcite inclusions, typically intergrown with pyrochlore and zircon. Sr-Ba-bearing pyrochlore is intergrown with strontianite, fluorite and baryte. Fine-grained baryte aggregates are observed interstitial to albite grains (Fig. 5). These textural observations can be used to suggest that the interaction of calcite carbonatite and nepheline syenite results in fluid alteration of the primary calcite and possibly released elements such as Sr, Ba, REE and Fe to form the secondary phases: strontianite, REE-fluorcarbonates, Ba-Sr-bearing pyrochlore, baryte and celestine.

In the calcite carbonatite 'zero' dyke (sample 269), burbankite always occurs as resorbed relicts (50–100 µm in size) in the central

https://doi.org/10.1180/mgm.2021.56 Published online by Cambridge University Press

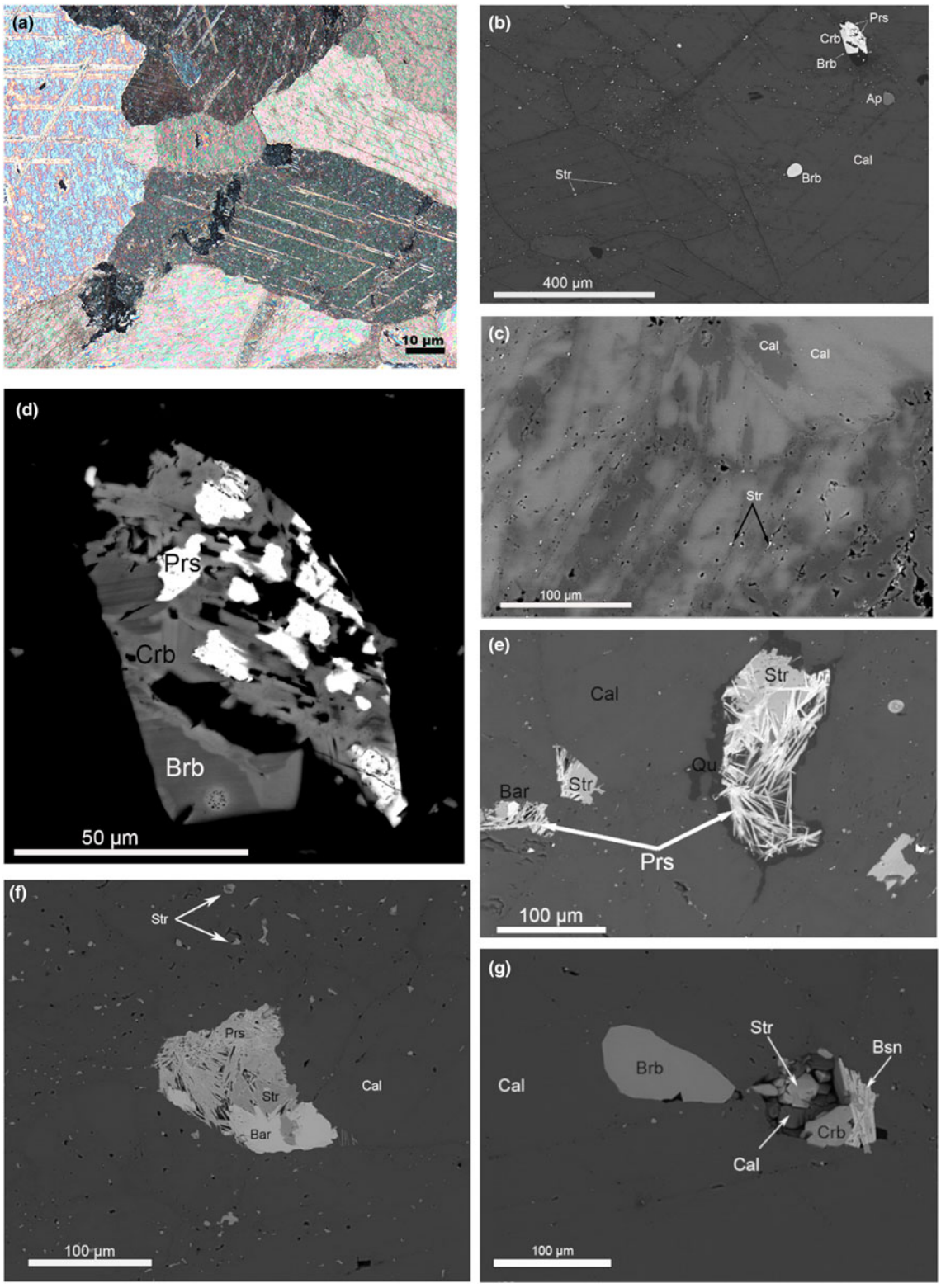

Fig. 4. (a) Calcite polysynthetic twins, sharp grain boundaries. Photograph in cross-polarised transmitted light. (b) Strontianite inclusions along cleavage planes of calcite. Dark areas along the cleavage planes are depleted in Sr (Table 2). BSE image. (c) Sr-bearing calcite (bright areas) replaced by Sr-poor calcite along the grain boundaries and cleavage planes (Table 2). BSE image. (d) Burbankite crystal resorbed and replaced by carbocernaite and bastnäsite. BSE image. (e) Dissolution cavity filled with strontianite, baryte, parisite and quartz – full pseudomorph after burbankite. BSE image. (f) Dissolution cavity filled with strontianite, baryte and parisite – full pseudomorph after burbankite. BSE image. (g) Slightly resorbed burbankite crystal and dissolution cavities filled with association of minerals: strontianite, calcite, carbocernaite and bastnäsite. BSE image. Abbreviations: Ap – apatite; Bar –baryte; Brb – burbankite; Bsn – bastnäsite; Cal – calcite; Crb –carbocernaite; Prs – parisite; Qu – quartz; Str – strontianite.

https://doi.org/10.1180/mgm.2021.56 Published online by Cambridge University Press

Table 2. Representative compositions (WDS data) for main rock-forming carbonates in Lofdal calcite carbonatites*.

Sample	Nam-326				Nam-269								
Area	centre		rim		centre			heterogeneous grains					
Mineral	calcite	calcite	calcite	calcite	calcite	calcite	calcite	ankerite	dolomite	ankerite	dolomite	ankerite	ankerite
Analysis	1	2	3	4	5	6	7	8	9	10	11	12	13
Wt.%													
Na_2O	0.05	0.08	b.d.	0.06	b.d.	b.d.	b.d.	b.d.	b.d.	b.d.	b.d.	b.d.	b.d.
MgO	0.09	0.08	0.15	0.09	0.12	0.11	0.09	4.34	8.33	7.68	9.46	4.03	3.79
CaO	52.37	52.73	53.69	53.39	52.41	52.58	52.54	29.96	29.16	29.16	29.34	29.34	29.16
MnO	1.13	1.14	1.17	1.04	1.11	1.14	1.12	4.90	5.28	4.32	6.06	4.57	4.37
FeO	1.05	1.15	0.99	0.90	1.07	1.12	1.09	18.18	13.28	15.40	10.92	19.12	20.13
SrO	1.65	1.46	0.43	0.83	2.11	2.09	2.02	0.71	0.83	0.47	0.53	0.76	0.70
BaO	b.d.	b.d.	b.d.	b.d.	0.08	b.d.	b.d.	b.d.	b.d.	b.d.	b.d.	b.d.	b.d.
CO_2	43.27	43.56	43.82	43.59	43.53	43.66	43.55	42.73	43.74	43.58	44.03	42.30	42.36
Total	99.61	100.21	100.26	99.90	100.43	100.70	100.42	100.82	100.63	100.61	100.34	100.11	100.51
Atoms per formula unit													
Na	0.002	0.003	-	0.002	-	-	-	-	-	-	-	-	-
Mg	0.002	0.002	0.004	0.002	0.003	0.003	0.002	0.222	0.416	0.385	0.469	0.208	0.195
Ca	0.950	0.950	0.962	0.961	0.945	0.945	0.947	1.100	1.046	1.050	1.046	1.089	1.080
Mn	0.016	0.016	0.017	0.015	0.016	0.016	0.016	0.142	0.150	0.123	0.171	0.134	0.128
Fe	0.015	0.016	0.014	0.013	0.015	0.016	0.015	0.521	0.372	0.433	0.304	0.554	0.582
Sr	0.016	0.014	0.004	0.008	0.021	0.020	0.020	0.014	0.016	0.009	0.010	0.015	0.014
Ba	-	-	-	-	0.001	-	-	-	-	-	-	-	-
Total	1.001	1.001	1.000	1.001	1.000	1.000	1.000	2.000	2.000	2.000	2.000	2.000	2.000

*Sample numbers: Nam-326 – Main Intrusion; Nam-269 – calcite carbonatite 'zero' dyke. The minerals were analysed by wavelength-dispersive X-ray spectrometry using JEOL JXA-8530F electron microprobe (settings in Supplementary material). All Fe expressed as FeO. CO_2 was calculated by stoichiometry, b.d. – below detection limit detection limits [ppm]: Na = 329, Mg = 366, Ca = 414, Mn = 638, Fe = 706, Sr = 512, Ba = 558. The proportion of cations was calculated on the basis of 1 $(CO_3)^{2-}$ group for calcite and 2 $(CO_3)^{2-}$ for dolomite–ankerite.

Table 3. Representative compositions (WDS data) for burbankite in Lofdal calcite carbonatites*.

Location	Main Intrusion									Carbonatite dyke					
Sample	Nam-08-58									Nam-269					
Analysis	3	6	7	8	11	12	13	14	15	16	20	22	24	25	29
Wt.%															
Na_2O	10.02	10.32	10.96	11.45	11.15	11.28	11.38	11.92	11.55	10.32	11.21	10.97	10.96	11.27	11.15
CaO	5.57	8.72	7.63	5.59	7.10	7.44	6.37	5.32	5.60	5.68	5.37	5.48	5.41	5.44	5.35
SrO	31.54	33.19	31.38	28.67	30.21	29.95	29.96	28.89	30.09	26.33	26.12	26.95	25.57	25.27	26.05
BaO	4.09	3.15	3.02	2.91	2.89	3.05	2.88	2.86	2.60	10.06	10.14	9.65	10.14	10.15	10.34
La_2O_3	5.48	3.66	4.48	6.55	4.49	5.25	5.60	6.38	6.12	4.68	4.69	4.68	4.88	4.98	4.95
Ce_2O_3	9.37	7.72	8.86	10.97	9.39	9.47	9.92	10.82	10.42	10.02	9.70	9.67	9.94	10.06	9.91
Pr_2O_3	0.47	0.48	0.58	0.58	0.65	0.58	0.58	0.59	0.57	0.61	0.63	0.67	0.62	0.57	0.58
Nd_2O_3	1.73	1.95	2.08	2.07	2.28	1.99	2.09	2.11	1.97	2.30	2.19	2.05	2.04	2.09	2.16
ThO_2	b.d.	b.d.	b.d.	b.d.	b.d.	b.d.	b.d.	b.d.	b.d.	b.d.	0.12	0.14	0.13	0.09	0.09
F	0.21	0.19	0.21	0.24	0.22	0.21	0.23	0.25	0.26	0.26	0.25	0.24	0.23	0.23	0.23
CO_2	32.67	34.49	34.15	33.36	33.65	34.15	33.68	33.45	33.50	32.63	32.85	32.94	32.59	32.79	32.98
$-O = F_2$	0.09	0.08	0.09	0.10	0.09	0.09	0.10	0.10	0.11	0.11	0.11	0.10	0.10	0.10	0.10
Total	101.04	103.78	103.27	102.28	101.94	103.27	102.61	102.48	102.57	102.79	103.18	103.34	102.41	102.83	103.68
Atoms per formula units calculated to 5 $(CO_3)^{2-}$ groups															
Na	2.178	2.125	2.278	2.436	2.352	2.346	2.399	2.531	2.448	2.246	2.422	2.364	2.387	2.440	2.400
Ca	0.669	0.992	0.877	0.658	0.828	0.855	0.742	0.624	0.656	0.683	0.642	0.653	0.652	0.651	0.636
Σ*A* site	2.847	3.116	3.155	3.094	3.181	3.201	3.141	3.155	3.103	2.930	3.064	3.017	3.039	3.090	3.036
Sr	2.050	2.043	1.951	1.825	1.906	1.863	1.889	1.834	1.908	1.713	1.689	1.738	1.666	1.636	1.678
Ba	0.180	0.131	0.127	0.125	0.123	0.128	0.123	0.123	0.111	0.442	0.443	0.420	0.447	0.444	0.450
La	0.227	0.143	0.177	0.265	0.180	0.207	0.225	0.258	0.247	0.194	0.193	0.192	0.202	0.205	0.203
Ce	0.384	0.300	0.348	0.441	0.374	0.372	0.395	0.434	0.417	0.412	0.396	0.394	0.409	0.411	0.403
Pr	0.019	0.018	0.023	0.023	0.026	0.022	0.023	0.024	0.023	0.025	0.026	0.027	0.025	0.023	0.024
Nd	0.069	0.074	0.080	0.081	0.089	0.076	0.081	0.083	0.077	0.092	0.087	0.082	0.082	0.083	0.086
Th	-	-	-	-	-	-	-	-	-	-	0.003	0.004	0.003	0.002	0.002
Σ*B* site	2.929	2.710	2.706	2.760	2.698	2.669	2.736	2.754	2.783	2.878	2.837	2.856	2.834	2.806	2.845
F	0.074	0.064	0.071	0.084	0.075	0.073	0.078	0.085	0.089	0.092	0.089	0.084	0.083	0.081	0.081

*Sample numbers: Nam-326, Nam-08-98 – Main Intrusion; Nam-269 – 'zero' dyke. CO_2 was calculated by stoichiometry. Burbankite samples were analysed by wavelength-dispersive X-ray spectrometry using a CAMECA SX-100 electron microprobe (probe settings in Supplementary material). b.d. – below detection, mean detection limits [ppm]: Na = 653, Sr = 369, Ca = 235, La = 619, Ce = 798, Pr = 648, Ba = 437, Nd = 869, Th = 607 and F = 196. Fe, Y, Sm, Gd, U and S were sought, though not detected in any of the grains.

https://doi.org/10.1180/mgm.2021.56 Published online by Cambridge University Press

Table 4. Representative compositions (WDS data) for carbocernaite in Lofdal calcite carbonatites*.

Location	Main Intrusion									
Sample	Nam-326									
Analysis	1	2	4	5	6	8	9	10	11	12
Wt.%										
Na_2O	3.33	2.66	3.10	2.71	3.02	3.42	3.50	3.40	3.37	3.37
CaO	16.46	21.12	13.74	13.37	13.58	16.70	16.45	16.72	17.04	16.38
FeO	b.d.	0.35	b.d.	b.d.	b.d.	b.d.	b.d.	b.d.	b.d.	b.d.
SrO	21.93	24.17	21.96	20.03	19.44	23.34	23.56	24.43	23.26	23.54
BaO	3.56	1.78	1.43	1.66	1.74	2.18	2.58	1.87	2.84	2.65
La_2O_3	6.46	4.96	9.64	9.48	9.89	7.13	6.78	6.88	5.72	6.08
Ce_2O_3	12.33	8.95	15.83	17.39	17.45	12.14	11.91	11.80	11.50	11.61
Nd_2O_3	4.01	2.33	3.77	4.41	4.63	3.42	3.98	3.14	4.05	4.05
Sm_2O_3	0.17	0.15	0.18	0.00	0.00	0.19	0.30	0.00	0.18	0.16
F	0.16	0.15	0.36	0.44	0.47	0.22	0.30	0.29	0.26	0.18
CO_2*	34.65	35.85	34.12	33.45	33.85	35.00	35.01	34.88	34.76	34.58
$-O = F_2$	0.07	0.06	0.15	0.19	0.20	0.09	0.12	0.12	0.11	0.08
Total	103.00	102.41	103.97	102.74	103.88	103.66	104.25	103.29	102.87	102.52
Atoms per formula units calculated to 2 $(CO_3)^{2-}$ groups										
Na	0.273	0.210	0.258	0.230	0.253	0.277	0.284	0.277	0.276	0.276
Ca	0.746	0.925	0.632	0.627	0.630	0.749	0.737	0.752	0.769	0.744
Σ*A* site	1.019	1.135	0.890	0.857	0.883	1.026	1.021	1.029	1.045	1.020
Fe	-	0.012	-	-	-	-	-	-	-	-
Sr	0.538	0.573	0.547	0.509	0.488	0.567	0.572	0.595	0.568	0.578
Ba	0.059	0.028	0.024	0.028	0.030	0.036	0.042	0.031	0.047	0.044
La	0.101	0.075	0.153	0.153	0.158	0.110	0.105	0.107	0.089	0.095
Ce	0.191	0.134	0.249	0.279	0.277	0.186	0.182	0.181	0.177	0.180
Nd	0.061	0.034	0.058	0.069	0.072	0.051	0.059	0.047	0.061	0.061
Sm	0.003	0.002	0.003	-	-	0.003	0.004	-	0.003	0.002
Σ*B* site	0.951	0.858	1.033	1.038	1.023	0.952	0.965	0.961	0.945	0.961
F	0.022	0.020	0.049	0.062	0.065	0.030	0.039	0.038	0.035	0.024

*All Fe expressed as FeO. CO_2 was calculated by stoichiometry. Carbocernaite samples were analysed by wavelength-dispersive X-ray spectrometry using a JEOL JXA-8530F electron microprobe (probe settings in Supplementary material). b.d. – below detection limit, mean detection limts [ppm]: Na = 475, Ca = 441, Fe = 868, Sr = 638, Fe = 660, Ba = 781, La = 2309, Ce = 1949, Nd = 1505, Sm = 1246 and F = 987. The proportion of cations are calculated on the basis of 2 $(CO_3)^{2-}$ groups.

part of polymineralic pseudomorphs (Fig. 6a–c). The pseudomorphs after burbankite in the dyke are complex. We have established several distinct assemblages of secondary minerals within pseudomorphs: (1) carbocernaite + strontianite + ancylite-(Ce) + baryte + barytocalcite + cordylite-(Ce); (2) ancylite-(Ce) + celestine + cordylite-(Ce); (3) ancylite-(Ce) + strontianite + baryte; (4) parisite-(Ce) + strontianite + baryte; and (5) parisite-(Ce) + celestine (Fig. 6a–c). All stages of burbankite alteration have been observed – from slightly resorbed burbankite crystals, replaced by carbocernaite (Fig. 4d) to thin rims of ancylite + strontianite mixture that penetrated into burbankite crystals (Fig. 6a) to full hexagonal pseudomorphs with a cavernous structure (Fig. 6b–c).

The pseudomorphs after burbankite in the 'zero' carbonatite dyke are observed in the following paragenesis: calcite; magnetite with ilmenite exsolutions; fluorite; phlogopite; fluorapatite; dolomite–ankerite. A banded texture is clearly observed in this carbonatite type (Fig. 7a). In areas close to the pseudomorphs, the rock-forming calcite has been altered, and has irregular patches of low-Sr secondary calcite replacing primary high-Sr calcite (as on Fig. 4c) together with dolomite–ankerite crystals (Fig. 7b). Such banded textures suggest fluid alteration of primary calcite carbonatite. This fluid according to the new mineral assemblage in the bands, was rich in F^-, K^+, Mg^{2+}, PO_4^{3-}, Ba^{2+} and SO_4^{2-}. A simplified paragenetic sequence for Lofdal calcite carbonatites is shown on Fig. 8.

Burbankite composition

All microprobe analyses of burbankite were recalculated on the basis of 5 $(CO_3)^{2-}$ groups. Generally, the microprobe analysis produced good stoichiometric compositions for burbankite, with no deficiency in the *A* site (Wall and Zaitsev, 2004). Effenberger *et al.* (1985), Belovitskaya *et al.* (2000) and Belovitskaya and Pekov (2004) suggest that there is an *A*-site cation deficiency, though this is also exactly the effect produced by Na migration during EPMA, to which burbankite is particularly sensitive. However, by comparing our results with published data, we can conclude that our microprobe analyses do not suffer from the effect of Na migration.

Burbankite compositions containing 0.7–1.5 atoms per formula unit (apfu) Sr and 0.4–1.0 apfu Ba in the *B* site together with 0.0–1.0 apfu Ca and 0.5–0.8 apfu REE are typical for carbonatite complexes (Belovitskaya and Pekov, 2004). Most of the Lofdal burbankite corresponds to burbankite *sensu stricto* (Table 3). There is one clear compositional trend; burbankite from the pseudomorphs is more enriched in Ba compared to burbankite from primary inclusions in calcite (Fig. 9a, Table 3). The maximum Ba content is 11.48 wt.% BaO (0.495 apfu) from pseudomorphs and the minimum content is 1.99 wt.% BaO (0.100 apfu) from inclusions. Other elements show minor variations within Lofdal burbankite (Fig. 9b,c), however no obvious compositional trend between inclusions and pseudomorphs can be observed. Comparison of the Lofdal burbankite compositions with burbankite from other localities (Fig. 9) shows that all of the Lofdal compositions are intermediate within the field of published data available for burbankite from carbonatites (Subbotin *et al.*, 1999, Wall and Zaitsev, 2004, Chakhmouradian and Dahlgren, 2021).

Carbocernaite replaces burbankite in dissolution cavities, veinlets and in pseudomorphs and is characterised by a homogeneous

https://doi.org/10.1180/mgm.2021.56 Published online by Cambridge University Press

Table 5. Representative compositions (WDS data) for cordylite-(Ce) in Lofdal calcite carbonatites*.

Location	Carbonatite dyke									
Sample	Nam-269									
Analysis	1	6	7	8	9	10	11	12	14	15
Wt.%										
Na_2O	2.68	2.51	2.62	2.68	2.59	2.77	2.37	2.71	2.66	2.78
CaO	2.61	2.61	2.94	2.70	2.92	2.55	3.64	2.60	2.82	2.50
FeO	b.d.	2.02	b.d.	0.18	b.d.	b.d.	b.d.	b.d.	b.d.	b.d.
SrO	2.99	3.07	3.75	3.07	4.05	2.86	4.53	3.09	3.40	2.97
Y_2O_3	b.d.	0.06	0.12	b.d.	0.05	b.d.	0.13	0.05	b.d.	0.05
BaO	24.09	19.94	24.68	23.92	21.98	24.83	23.49	24.59	24.62	24.71
La_2O_3	13.95	13.55	13.06	12.97	13.15	12.57	12.62	13.27	13.01	13.33
Ce_2O_3	21.44	20.73	20.95	20.80	21.59	21.28	19.65	20.99	20.75	21.32
Pr_2O_3	0.820	0.93	0.711	0.81	0.89	0.88	0.78	0.78	0.80	0.75
Nd_2O_3	5.31	5.37	5.58	5.75	5.87	5.980	5.77	5.76	5.539	5.58
Sm_2O_3	0.38	0.40	0.53	0.50	0.53	0.58	0.60	0.47	0.54	0.41
Gd_2O_3	0.39	0.47	0.45	0.52	0.49	0.54	0.59	0.46	0.41	0.40
ThO_2	0.66	0.62	0.63	0.70	0.74	0.80	0.93	0.75	0.71	0.80
UO_2	0.14	0.09	0.10	0.13	0.12	0.09	0.15	0.14	0.11	0.12
F	2.54	3.04	2.65	2.55	2.61	2.96	2.53	2.98	2.40	2.65
SO_3	0.34	0.25	b.d.	b.d.	b.d.	b.d.	b.d.	b.d.	b.d.	b.d.
CO_2*	26.99	25.89	26.64	26.21	26.50	25.95	26.74	25.93	26.56	26.31
$-O = F_2$	1.07	1.28	1.12	1.07	1.10	1.24	1.06	1.26	1.01	1.12
Total	104.25	100.27	104.28	102.41	102.99	103.40	103.45	103.31	103.31	103.54
Atoms per formula units calculated to 4 $(CO_3)^{2-}$ groups										
Na	0.563	0.552	0.558	0.580	0.555	0.605	0.503	0.593	0.568	0.599
Ca	0.304	0.316	0.346	0.323	0.346	0.308	0.427	0.315	0.333	0.298
Σ*A* site	0.867	0.868	0.904	0.904	0.901	0.914	0.930	0.907	0.901	0.898
Fe	-	0.191	-	0.017	-	-	-	-	-	-
Sr	0.188	0.201	0.239	0.199	0.259	0.187	0.288	0.202	0.217	0.192
Y	-	0.003	0.007	-	0.003	-	0.008	0.003	-	0.003
Ba	1.024	0.885	1.064	1.048	0.952	1.099	1.008	1.088	1.064	1.078
La	0.558	0.566	0.530	0.535	0.536	0.524	0.510	0.553	0.529	0.547
Ce	0.852	0.859	0.844	0.852	0.874	0.879	0.788	0.868	0.838	0.869
Pr	0.032	0.038	0.029	0.033	0.036	0.036	0.031	0.032	0.032	0.030
Nd	0.206	0.217	0.219	0.230	0.232	0.241	0.226	0.232	0.218	0.222
Sm	0.014	0.016	0.020	0.019	0.020	0.023	0.023	0.018	0.020	0.016
Gd	0.014	0.018	0.016	0.019	0.018	0.020	0.021	0.017	0.015	0.015
Th	0.016	0.016	0.016	0.018	0.019	0.021	0.023	0.019	0.018	0.020
U	0.003	0.002	0.002	0.003	0.003	0.002	0.004	0.003	0.003	0.003
Σ*B* site	2.909	3.012	2.985	2.972	2.952	3.032	2.929	3.037	2.955	2.995
F	0.871	1.089	0.923	0.901	0.914	1.056	0.876	1.067	0.839	0.934
S	0.028	0.021	-	-	-	-	-	-	-	-

*All Fe expressed as FeO. CO_2 was calculated by stoichiometry. The cordylite samples were analysed by wavelength-dispersive X-ray spectrometry using a JEOL JXA-8530F electron microprobe (probe settings in Supplementary material). b.d. – below detection limit, mean detection limts [ppm]: Na = 301, Ca = 227, Fe = 829, Sr = 228, Y = 350, Ba = 507, La = 1167, Ce = 1124, Nd = 1219, Sm = 1018, Gd = 761, Th = 527, U = 429, F = 574 and S = 430. The proportion of cations are calculated on the basis of 4 $(CO_3)^{2-}$ groups.

composition (Table 4), similar to the compositions reported for this mineral worldwide (Wall *et al.*, 1993; Zaitsev *et al.*, 1998; Wall and Zaitsev, 2004; Chakhmouradian *et al.*, 2017).

The composition of cordylite is shown in Table 5. Ba-REE-fluorocarbonates are rare in carbonatites and WDS analyses for cordylite have been reported from just a few localities: Khibiny, Kola Peninsula, Russia; Wicheeda, British Columbia; Palabora, South Africa; and Montviel, Abitibi, Canada (Zaitsev *et al.*, 1998; Dalsin *et al.*, 2015; Nadeau *et al.*, 2015; Giebel *et al.*, 2017). Cordylite from Lofdal is characterised by similar variations in composition to cordylite from these four localities and corresponds to cordylite-(Ce). In dolomite carbonatite of Biraya, East Siberia La-dominated cordylite appears as a rock-forming mineral (Mills *et al.*, 2012).

Raman spectroscopy

The minerals visible on BSE images (Fig. 6b) were investigated using Raman spectroscopy. Raman micro-spectroscopy can be used for identification of carbonates with a spatial resolution of ~1 μm (Herman *et al.*, 1987), hence the components of the polymineralic pseudomorphs (Fig. 6a–c) could be distinguished successfully even though they have a small grain size (Fig. 10b). Burbankite, carbocernaite, strontianite, ancylite, cordylite, baryte and barytocalcite were identified by comparison with spectra of well-characterised mineral reference materials from the BGR mineral collection and published Raman spectra (Fig. 10a–c).

Raman micro-spectroscopy is also especially helpful to differentiate between burbankite and carbocernaite (Moore *et al.*, 2015; Chakhmouradian *et al.*, 2017; Chakhmouradian and Dahlgren, 2021). Burbankite inclusions from primary calcite carbonatite of the Main Intrusion, resorbed grains and relicts of burbankite from the pseudomorphs as well as all replacement phases after burbankite were examined by Raman spectroscopy using the same instrumental parameters (see above). All Raman measurements of the Lofdal burbankite samples and comparison with reference REE carbonates from the authors' own and BGR collections show that the ovoid inclusions, hexagonal crystals

https://doi.org/10.1180/mgm.2021.56 Published online by Cambridge University Press

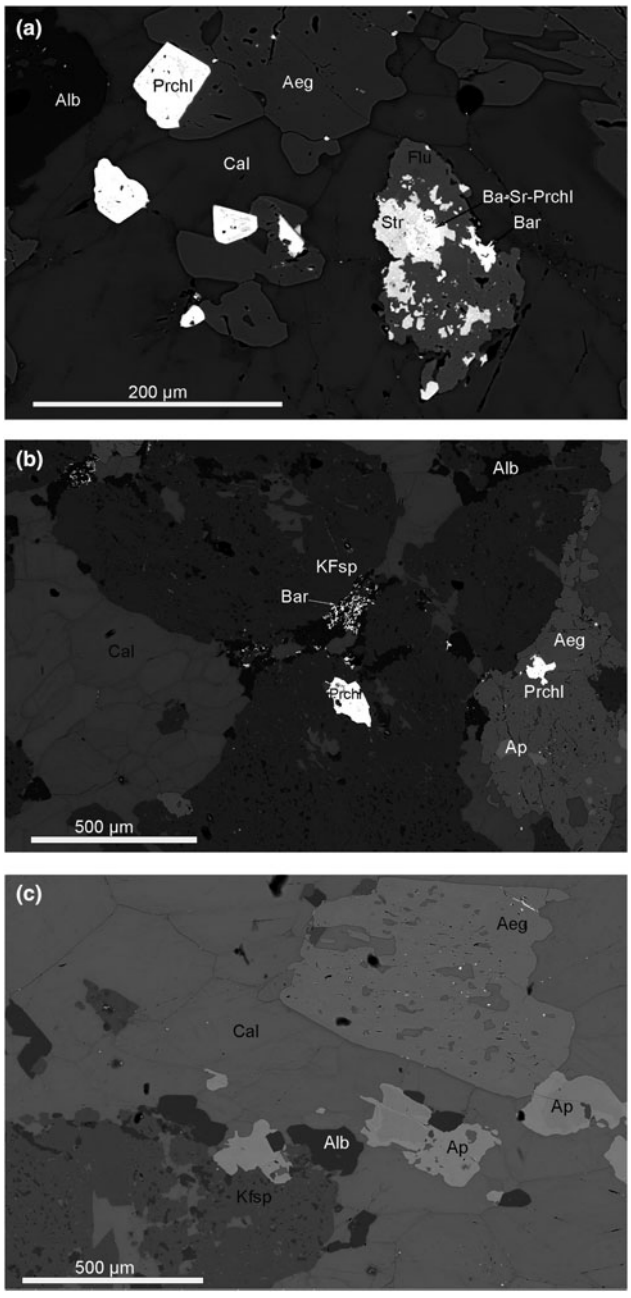

Fig. 5. (a) Aegirine–augite (Aeg), albite (Alb) and fluorite (Flu) in calcite carbonatite close to the contact with nepheline syenite. Alteration of calcite (Cal) along grain boundaries and cleavage planes. Aegirine–augite contains pyrochlore (Prchl) inclusions. Ba-Sr-bearing Pyrochlore (Ba-Sr-Prchl) intergrowths with strontianite (Str), fluorite and baryte (Bar) in late subsolidus association. BSE image. (b) Poikilitic inclusions of calcite in aegirine–augite and K-feldspar (KFsp) crystals. Aegirine–augite and K-feldspar contain pyrochlore and apatite (Ap) inclusions. Fine-grained baryte aggregates interstitial between albite grains. BSE image. (c) Poikilitic crystals of aegirine–augite, K-feldspar with calcite inclusions in association with zoned fluorapatite and albite in calcite carbonatite. BSE image.

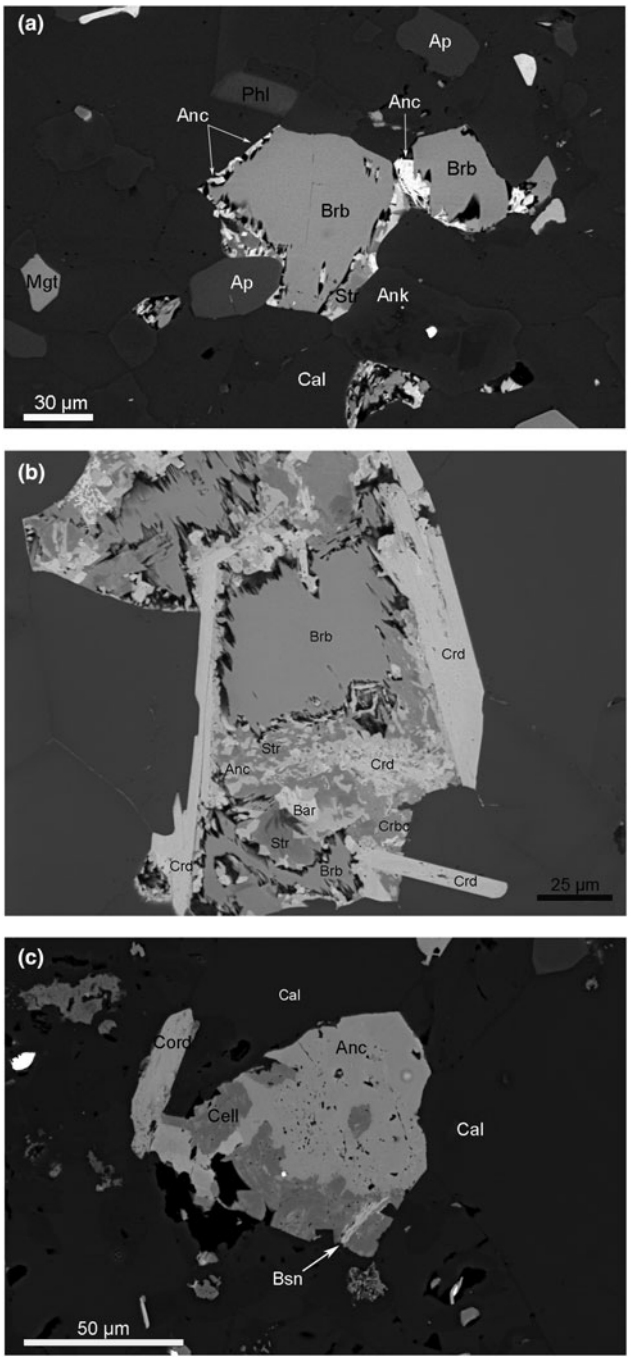

Fig. 6. (a) Hexagonal polymineralic pseudomorphs after burbankite. Resorbed relict of burbankite (Brb) replaced by ancylite (Anc) and strontianite (Str). The pseudomorphs are associated with calcite (Cal), magnetite (Mgt), fluorite, phlogopite (Phl), fluorapatite (Ap), ankerite (Ank). BSE image. (b) Complex polymineralic pseudomorphs after burbankite (Brb): the last one is replaced by carbocernaite (Crbc), strontianite (Str), ancylite (Anc) and overgrown with cordylite (Crd). BSE image. (c) Full pseudomorph after burbankite: celestine (Cell), ancylite (Anc), bastnäsite (Bsn), cordylite (Cord). BSE images.

and relicts of precursor mineral in the hexagonal pseudomorphs are identical to well-characterised burbankite from Khibiny, Kola Peninsula, Russia (Fig. 10a). All six samples of Lofdal burbankite measured with a 633 nm laser produced Raman spectra with several consistent features: an intensive symmetric C–O stretching mode – the peak at 1080 cm^{-1}, weak out-of-plane and in-plane C–O bending signals at 860–875 and 695–714, respectively, and weak asymmetric C–O bending and lattice mode between 150 and 280 cm^{-1}. The same peaks were also observed in burbankite from Khibiny (our unpublished data) and from Fen, Norway (Chakhmouradian and Dahlgren, 2021). Carbocernaite and burbankitehave similar compositions but can be distinguished easily by their Raman spectra using the split

https://doi.org/10.1180/mgm.2021.56 Published online by Cambridge University Press

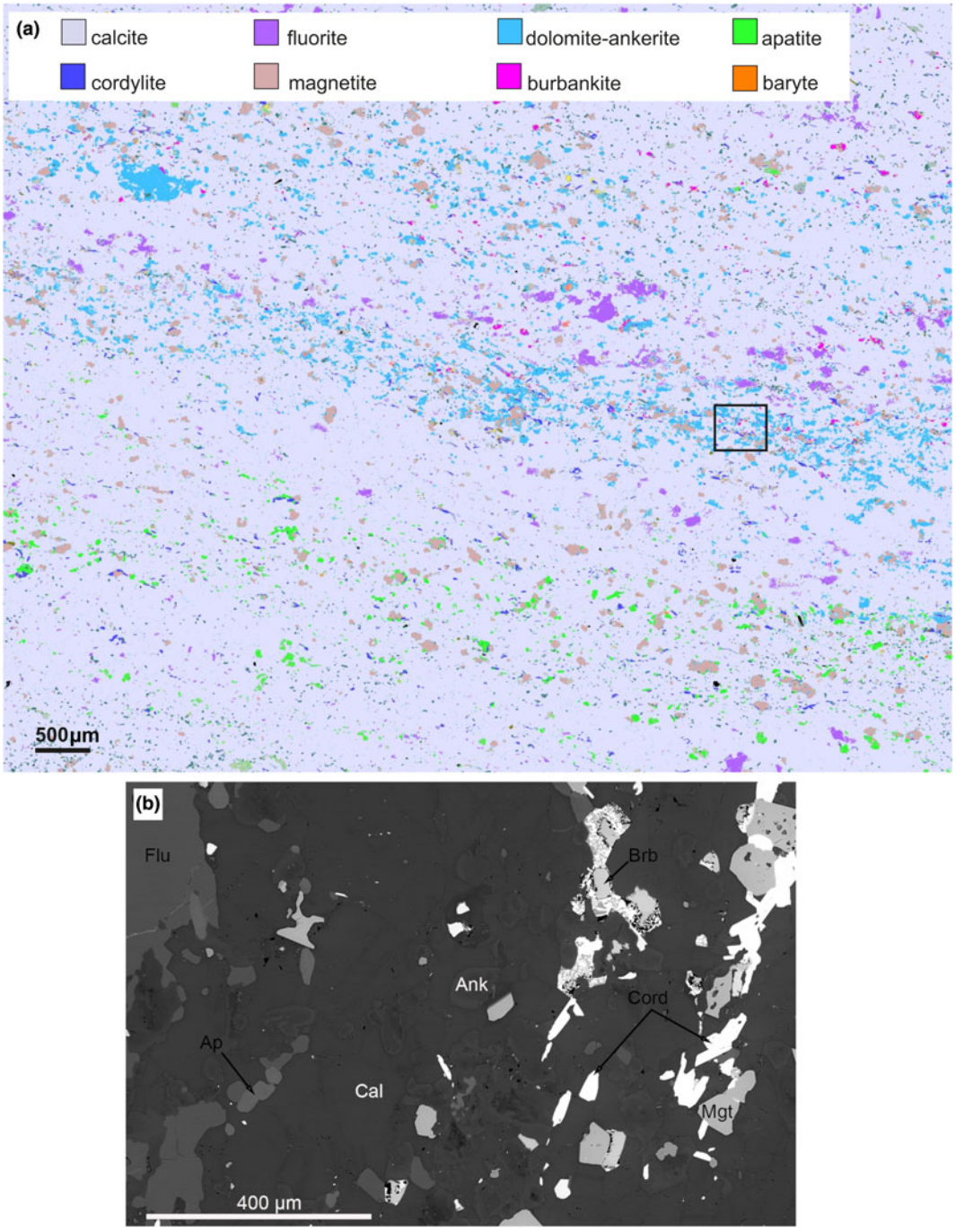

Fig. 7. (a) Modal mineralogy of calcite carbonatite with pseudomorphs after burbankite (sample Nam-269). For colour-codes see the legend. Note the banded texture of the carbonatite and the association of dolomite–ankerite and fluorite with pseudomorphs after burbankite. Mineral-distribution map from BSE-EDS using *Mineralogic* (Zeiss). The black frame indicates the area in (b), shown in BSE. The area shows the appearance of ankerite (Ank) crystals close to pseudomorphs after burbankite (Brb). Mgt – magnetite, Flu – fluorite, Ap – apatite, Cal – calcite, Cord – cordylite.

peak between ~1070 and 1100 cm^{-1} in the carbocernaite spectrum. This carbocernaite feature was first reported from Bear Lodge carbonatites, Wyoming, USA (Chakhmouradian *et al.*, 2017). We have compared the carbocernaite Raman spectra from Lofdal with the spectra of the Bear Lodge specimen. The split peak at ~1071, 1087 and 1097 cm^{-1} is present in both spectra. The different intensities of the two sides of the split peak are probably related to the variable compositions of carbocernaite at Lofdal (Table 4, an. 6, 8 and Fig. 10c).

Discussion

Burbankite-group minerals occur in different types of rocks: carbonatites; alkali-carbonate-bearing hydrothermal veins; and in natrolite–microcline or pectolite–natrolite-feldspar veinlets in nepheline syenites and melteigite–urtite (Zaitsev *et al.*, 1998; Subbotin *et al.*, 1999; Wall and Zaitsev, 2004; Yakovenchuk *et al.*, 2005; Moore *et al.*, 2015; Chakhmouradian *et. al.*, 2017). In carbonatites the burbankite-group minerals are usually early

https://doi.org/10.1180/mgm.2021.56 Published online by Cambridge University Press

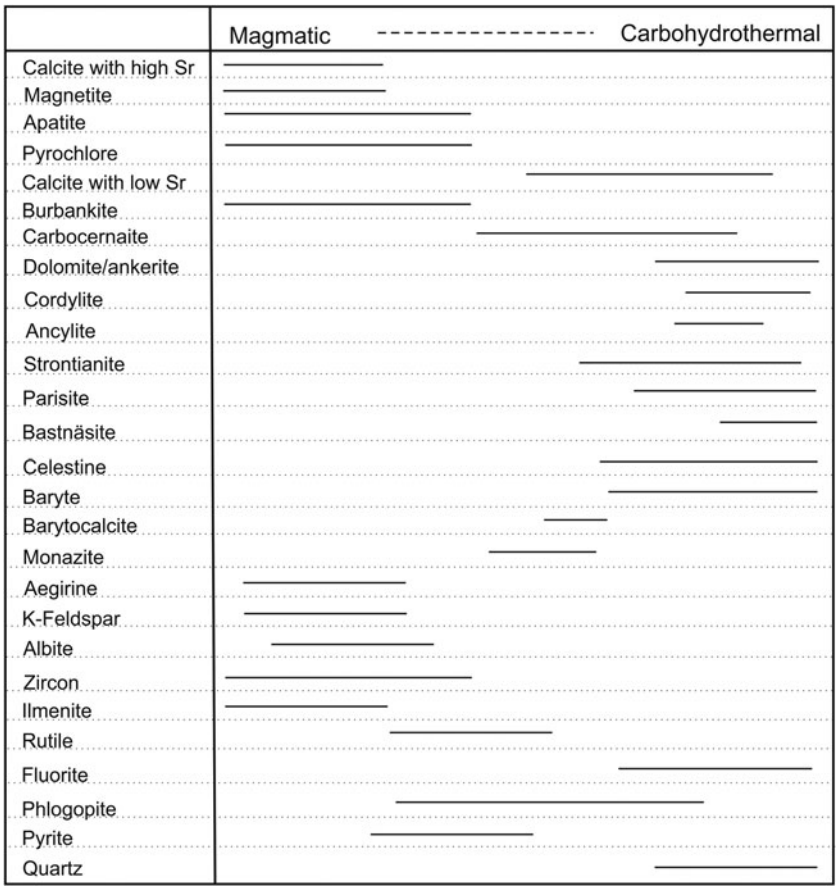

Fig. 8. Simplified paragenetic sequence of the Lofdal calcite carbonatite.

phases formed at high-temperatures, whereas in nepheline syenites they are formed during hydrothermal stages at low temperatures, representing different CO_2 regimes (Belovitskaya and Pekov, 2004).

In carbonatite complexes, three burbankite-group minerals, burbankite, calcioburbankite and khanneshite have been reported. Both burbankite and calcioburbankite have been reported in early calcite carbonatites as well as in late hydrothermal–metasomatic dolomite–calcite carbonatites (Subbotin *et al.*, 1999).

Khanneshite has been reported from the Afrikanda complex, Kola Peninsula, Russia (Zaitsev and Chakhmouradian, 2002); the Khanneshin carbonatite, southern Afghanistan (Tucker *et al.*, 2012); and Khibiny carbonatites, Kola Peninsula (Pekov *et al.*, 1998). Primary burbankite has been described in a few carbonatite complexes worldwide (Zaitsev *et al.*, 1997, 1998, 2002; Wall *et al.*, 2001; Chakmouradian *et al.*, 2016; Chakhmouradian and Dahlgren, 2021). Burbankite together with other Na-bearing carbonates was reported as primary inclusions in rock-forming minerals (magnetite and apatite) in carbonatites from Afrikanda and Sallanlatvi in the Kola Peninsula (Zaitsev and Chakhmouradian, 2002; Zaitsev *et al.*, 2004). Examples of fresh burbankite and polymineralic pseudomorphs were described by Zaisev *et al.* (2002) who provided isotopic evidence that burbankite crystallised from a primary, alkali-rich carbonatite melt. Blebs in rock-forming carbonate have been reported by Wall (2004) and Chakhmouradian and Dahlgren (2021).

Bühn *et al.* (1999) detected burbankite in fluid inclusions within quartzite related to the Kalkfeld carbonatite complex, Namibia. They proposed that this burbankite had crystallised directly from an alkali-rich carbonatite melt before alkalis were lost during wall-rock fenitisation. Dowman *et al.* (2017) found burbankite in fluid inclusions in quartz from fenite around the Chilwa Island carbonatite, Malawi and interpreted this as evidence of REE fluid mobility in the fenitising solutions.

Anenburg *et al.* (2020) found that burbankite-group minerals crystallised at the transition between igneous carbonate and fluid in experiments with Na and REE-bearing carbonatite compositions. This timing of burbankite formation is consistent with many observations, although these experiments did not produce blebs or crystals of burbankite in calcite. Possible explanations are that the crystallisaton of the calcite carbonatite was a closed system trapping the burbankite, or that with different conditions, such as lower water content but still high sodium, burbankite will crystallise earlier during the magmatic stage.

The interpreted paragenetic sequence for the Lofdal calcite carbonatites in Fig. 8 demonstrates the role of burbankite, high-Sr calcite, magnetite, ilmenite, apatite, pyrochlore, aegirine, K-feldspar and zircon as early magmatic phases. In the transition from magmatic to carbohydrothermal activity burbankite is replaced by carbocernaite and parisite (Fig. 4d). The degree of alteration ranges from a partial replacement to complete pseudomorphs with no relict fragments of burbankite (Fig. 4e,f). Carbocernaite relict grains also occur in peripheral parts of the pseudomorphs (Fig. 6b). The transition environment is interpreted similarly to the magmatic–hydrothermal transition observed in granite systems (e.g. Audétat *et al.*, 2000, Halter and Webster, 2004). Strontianite, low-Sr calcite, phlogopite, rutile, barytocalcite, pyrite and monazite continued to crystallise in the

https://doi.org/10.1180/mgm.2021.56 Published online by Cambridge University Press

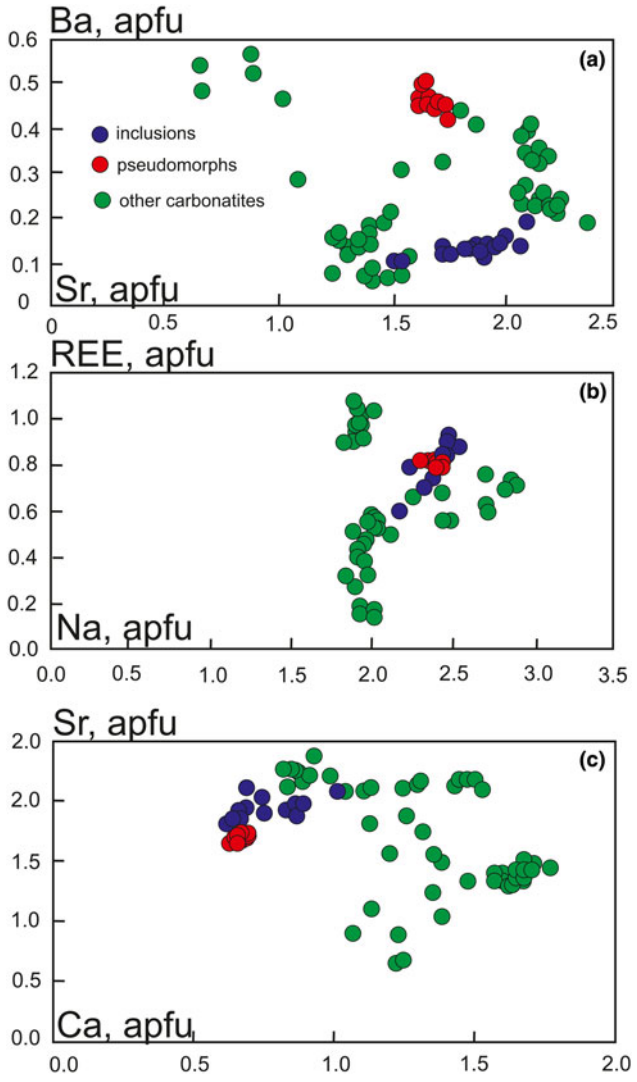

Fig. 9. Compositional variation of Lofdal burbankite inclusions (red circles) and relicts of burbankite from the pseudomorphs (blue circles) compared to available published data (green circles) for burbankite from carbonatites (Subbotin *et al.*, 1999, Wall and Zaitsev, 2004, Chakhmouradian and Dahlgren, 2021 and the authors unpublished data on burbankite from Cerro-Sapo, Bolivia).

transitional environment. Burbankite may be destabilised when fluids exsolve from the magma and the most soluble components, notably Na, are dissolved away. These fluids react with previously crystallised material, producing pseudomorphs (Wall, 2004). Thus at the carbohydrothermal stage, burbankite was replaced by bastnäsite, parisite, ancylite, strontianite, celestine, baryte and cordylite with the appearance of abundant dolomite–ankerite, phlogopite, fluorite and rare quartz.

Pseudomorphs after burbankite, similar to those in Khibiny carbonatites, have been reported from several carbonatite localities: Gornoe Ozero in East Siberia (Zdorik, 1966); Vuorijarvi, Kola Peninsula (Kapustin, 1980; Subbotin *et al.*, 1999, Wall and Zaitsev, 2004); and Bear Lodge (Moore *et al.*, 2015; Chakhmouradian *et al.*, 2017). In these localities the evidence for the late-stage subsolidus origin of ancylite and synchysite after burbankite are the complete hexagonal pseudomorphs and abundant relict grains of burbankite in mineral intergrowths. Similar pseudomorphs, interpreted as produced by a volume-for-volume replacement mechanism (Zaitsev *et al.*, 1998, Zaitsev *et al.*, 2002) are found at Lofdal. We agree with Wall and Mariano (1996), Zaitsev *et al.* (1998) and Wall *et al.* (2001) that replacement of burbankite and the formation of hexagonal pseudomorphs with a cavernous structure involves a late-stage reaction between water-bearing fluids and burbankite. Such hexagonal LREE-Sr-Ba-rich pseudomorphs were observed in several carbonatite localities though commonly without relict fragments of a precursor mineral; for example at Kangankunde, Malawi and Sallanlatvi, Kola Peninsula (Wall and Mariano, 1996; Zaitsev *et al.*, 2004). The absence of a precursor mineral in the pseudomorphs probably can be explained by the susceptibility of burbankite to hydrothermal alteration such that the burbankite was altered completely to the new LREE-Sr-Ba-mineral association as a result of re-working of primary carbonatite with the hydrothermal fluid (Wall and Mariano, 1996). In Sallanlatvi, burbankite was found in fluid inclusions within magnetite in calcite carbonatites (Zaitsev *et al.*, 2004).

The observed textures of Lofdal calcite carbonatites from the Main Intrusion (Fig. 3, 4) are interpreted as igneous textures (Chakmouradian *et al.*, 2016). Burbankite inclusions in the calcite carbonatite are abundant and make up to 0.5 vol.% of the modal mineralogy of the rock. The distribution of burbankite ovoid inclusions and hexagonal crystals in the calcite matrix is not controlled crystallographically, nor confined to cleavage planes or fractures. The surrounding calcite is enriched in Sr (up to 2.11 wt.% SrO, Table 2) and there is no evidence of calcite or burbankite recrystallisation in this type of rock. All these compositional and textural features of Lofdal calcite carbonatites argue that burbankite has been formed syngenetically with its host carbonate at the early stage of carbonatite evolution. The early crystallisation of burbankite provides evidence that the carbonatitic magma was enriched in Na, Sr, Ba and LREE.

The isotopic characteristics of calcite carbonatite of the Lofdal Main Intrusion indicate that the source of the carbonatitic magma was in Enriched Mantle I reservoir (Bell and Blenkinsop, 1987; Bell and Tilton, 2001). The initial $^{87}Sr/^{86}Sr$ ratio of calcite carbonatite is 0.70274 and the initial $^{143}Nd/^{144}Nd$ ratio is 0.512227 with ϵNd_t of 2.4 (whole-rock data for sample 08-58 – calcite carbonatite with burbankite inclusions – from Do Cabo *et al.*, 2011). Carbon and oxygen isotopic compositions of the same sample: ($\delta^{13}C_{V\text{-}PDB} = -5.72‰$, $\delta^{18}O_{V\text{-}SMOW} = 5.58‰$) plot in the primary carbonate field proposed by Keller and Zaitsev (2006) and thus support our interpretation.

Carbonatites are more likely than silicate rocks to be susceptible to subsolidus alteration and, hence, few of these rocks retain their magmatic characteristics (Chakhmouradian *et al.*, 2016, p. 337). The carbonatites of the Lofdal Main Intrusion are no exception to this observation as at least some areas of the carbonatites have undergone this style of alteration. We have observed local replacement textures of primary calcite carbonatites (e.g. sample 326, 269). Calcite in the peripheral parts of the crystals and along cleavage planes is characterised by lower Sr contents and appearance of numerous tiny strontianite grains along fluid passageways – cleavage planes or fractures, and along grain boundaries (Fig. 4b). The common presence of the REE hydrocarbonate–ancylite–sulfates (baryte and celestine), in this paragenesis are clear indications of fluid involvement (Cooper *et al.*, 2015).

Significant variations in Sr or REE between burbankite inclusions and burbankite from the pseudomorphs were not detected. The fact that burbankite from the pseudomorphs is more

https://doi.org/10.1180/mgm.2021.56 Published online by Cambridge University Press

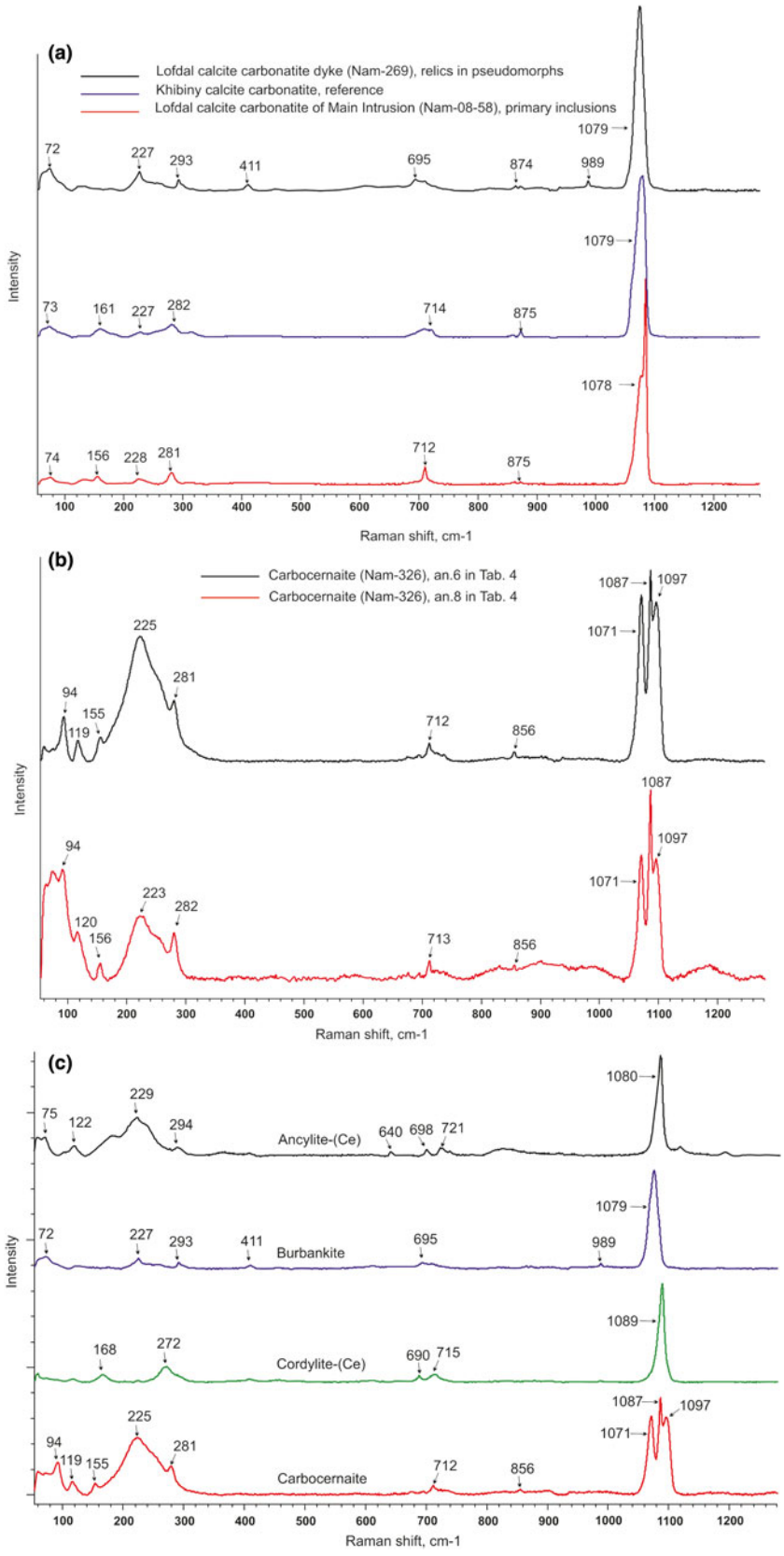

Fig. 10. (a) Representative Raman spectra of burbankite inclusions and relics in pseudomorphs from Lofdal and reference material from Khibiny, Kola Peninsula. (b) Representative Raman spectra of burbankite, ancylite-(Ce), cordylite-(Ce) and carbocernaite from the pseudomorphs after burbankite, Lofdal, Namibia, (c) Representative Raman spectra of carbocernaite from the pseudomorphs after burbankite, Lofdal, Namibia. The intensity difference of the triple peak at ~1080 is probably caused by variation of composition (Table 4, an. 6, 8). All Raman spectra were measured with a 633 nm laser.

enriched in Ba compared to burbankite from primary inclusions in calcite (Fig. 9a, Table 3) contradicts the observation for burbankite in Bear Lodge (Moore *et al.*, 2015, p.514) where the early burbankite is more enriched in Ba than the late variety.

It is known that burbankite is not a stable mineral. With decreasing alkalinity it becomes unstable and at hydrothermal conditions it is easily replaced by a whole series of secondary minerals, such as alkali-free carbonates of REE, Sr, Ba and Ca

https://doi.org/10.1180/mgm.2021.56 Published online by Cambridge University Press

(Belovitskaya and Pekov, 2004 and references therein). This is consistent with our observations: alteration of the primary burbankite into secondary carbocernaite, appearance of hexagonal pseudomorphs with different mineral composition: ancylite, strontianite, baryte, celestine, parisite and numerous dissolution cavities with similar mineral assemblages ± quartz. All these observed alterations indicate changes in the alkalinity regime of the evolved carbo-hydrothermal fluid due to the loss of Na, probably to fenite aureoles. There are abundant albitites in Area 4 at the contact of carbonatite dykes and alkaline rocks at Lofdal (Williams-Jones *et al.*, 2015). As a result, we observe replacement of burbankite with the new REE-Sr-Ba-bearing mineral assemblage. In fenitisation, the fluids released from the cooling magma migrate through the crystallised surrounding rocks, causing intense metasomatic reactions, hydrothermal alteration, mobilisation of rare earth and high-field-strength elements and formation of secondary mineral assemblages at the expense of the original minerals (Broom-Fendley *et al.*, 2017; Zaitsev *et al.*, 2002). Thus, the growth of the new REE-Sr-Ba-bearing mineral assemblage probably resulted from the breakdown of magmatic minerals calcite and burbankite, releasing REE, Sr and Ba. Oxidation of primary minor pyrite present in calcite carbonatite by the hydrothermal fluid probably enabled crystallisation of Sr- and Ba-sulfates at the end of the process, as was also assumed for the Okorusu carbonatite complex (Cangelosi *et al.*, 2020). A transition from secondary marcasite after pyrite to baryte in the Bear Lodge carbonatite was also discussed by Chakhmouradian *et al.* (2017).

The appearance of abundant fluorite in association with pseudomorphs after burbankite is indicative that F probably played an important role in the decomposition of REE minerals. The role of fluorine has been demonstrated in many carbonatite complexes (Simonneti and Bell, 1995; Bühn *et al.*, 2003; Xu *et al.*, 2011) although recent experimental studies of hydrothermal systems (Williams-Jones *et al.*, 2012; Migdisov *et al.*, 2016) have suggested that, although fluorine is the strongest REE-binding ligand, the presence of fluorine in hydrothermal solutions, rather than facilitating REE transport causes precipitation of F-bearing REE carbonate or phosphate minerals (Migdisov and Williams-Jones, 2008; Migdisov *et al.*, 2009; 2016; Williams-Jones *et al.*, 2012). If the REE are transported as sulfate complexes, precipitation of sulfates, e.g. baryte, will induce precipitation of REE minerals. This statement correlates with our observation in Lofdal calcite carbonatites of the Main Intrusion that abundant baryte and celestine appear at the last stages of REE-mineral crystallisation, in dissolution cavities, veinlets and in pseudomorphs after burbankite.

Conclusions

Although the Lofdal alkaline carbonatite complex is best known for its xenotime content and HREE enrichment, there is also more typical occurrence of LREE-enriched calcite carbonatite, with abundant early forming burbankite blebs, occurring as hexagonal crystals and their subsequent pseudomorphs. These carbonatites do not contain xenotime. The early crystallisation of burbankite indicates that the carbonatitic magma was enriched in Na, Sr, Ba, and LREE. The isotope geochemistry of the calcite carbonatite is consistent with a mantle origin of the rock.

The primary minerals in the Main Intrusion calcite carbonatite, and especially nearby dykes. were partly-overprinted by hydrothermal fluids enriched in F^-, SO_4^{2-} and CO_3^{2-}. This alteration redistributed REE, Na, Sr and Ba to form a new mineral assemblage. Varying degrees of burbankite alteration have been observed, culminating in complete pseudomorphs in the dyke, which consist of carbocernaite, ancylite, bastnäsite, strontianite, celestine, parisite, cordylite and baryte. The fluid reworking of the carbonatites probably released Na into contact fenite aureoles.

The occurrence of abundant fluorite in association with pseudomorphs after burbankite suggests that fluorine probably plays an important role in the breakdown of REE complexes and subsequent precipitation of the REE mineral assemblage.

There is no direct relationship between the xenotime, including the deposit in Area 4, at Lofdal and the burbankite in the calcite carbonatites of the Main Intrusion, however the xenotime-bearing deposit in Area 4 is associated with albitite, and together with the abundant burbankite blebs in the magmatic calcite carbonatite, this indicates the sodium-rich nature of the Lofdal system overall, which may have promoted REE mobility.

Acknowledgements. We are grateful to the Namibia Geological Survey and Rainer Ellmies for their help with organising access to the Lofdal area and supporting us in the field. The manuscript was improved by the contributions of two anonymous referees and guest editors A.R. Chakhmouradian and A.N. Zaitsev. We are grateful to R.H. Mitchell for editorial handling. A.N. Zaitsev is thanked for providing a burbankite reference sample from Khibiny. We thank BGR colleagues D. Henry for sample preparation, F. Korte and H. Lorenz for geochemical analysis, F. Henjes-Kunst and P. Königer for the isotopic study, C. Whörl for his help with microprobe analysis, A. Marx and K.Berkh for their help with Raman spectroscopy analysis.

Supplementary material. To view supplementary material for this article, please visit https://doi.org/10.1180/mgm.2021.56

References

Anenburg M. Mavrogenes J.A., Frigo C. and Wall F. (2020) Rare earth element mobility in and around carbonatites controlled by sodium, potassium, and silica. *Science Advances*, **6**, eabb6570.

Audétat A., Gunther D. and Heinrich C.A. (2000) Magmatic-hydrothermal evolution in a fractionating granite: a microchemical study of the Sn-W-F-mineralised Mole granite (Australia). *Geochimica et Cosmochimica Acta*, **64**, 3373–3393.

Bell K. and Blenkinsop J. (1987) Nd and Sr isotopic compositions of East African carbonatites: Implications for mantle heterogeneity. *Geology*, **15**, 99–102.

Bell K. and Tilton G.R. (2001) Nd, Pb and Sr isotopic compositions of East African carbonatites: evidence for mantle mixing and plume inhomogeneity. *Journal of Petrology*, **42**, 1927–1945.

Belovitskaya Yu.V. and Pekov I.V. (2004) Genetic mineralogy of the burbankite group. *New Data Minerals*, **39**, 50–64.

Belovitskaya Yu.V., Pekov I.V. and Kabalov Yu.K. (2000) Refinement of the crystal structures of low rare earth and 'typical' burbankites by Rietveld method. *Kristallografiya*, **1**, 32–35 [in Russian].

Bodeving S., Williams-Jones A.E. and Swinde S. (2017) Carbonate–silicate melt immiscibility, REE mineralising fluids, and the evolution of the Lofdal intrusive suite, Namibia. *Lithos*, **268–271**, 383–398.

Borodin L.S. and Kapustin Yu.L. (1962) Burbankite, the first find in USSR. *Doklady Akademii Nauk SSSR*, **147**, 462–465 [in Russian].

Broom-Fendley S., Brady A.E., Wall F., Gunn G. and Dawes W. (2017) REE minerals at the Songwe Hill carbonatite, Malawi: HREE-enrichment in late-stage apatite. *Ore Geology Reviews*, **81**, 23–41.

Bühn B., Rankin A., Radtke M., Haller M. and Knöchel A. (1999) Burbankite, a (Sr, REE, Na, Ca) - carbonate in fluid inclusions from carbonatite-derived fluids: Identification and characterization using Laser Raman spectroscopy, SEM-EDX, and synchrotron micro-XRF analysis. *American Mineralogist*, **84**, 1117–1125.

Bühn B., Schneider J., Dulski P. and Rankin A.H. (2003) Fluid-rock interaction during progressive migration of carbonatitic fluids, derived from small-scale trace element and Sr, Pb isotope distribution in hydrothermal fluorite. *Geochimica et Cosmochimica Acta*, **67**, 4577–4595.

Cangelosi D., Broom-Fendley S., Banks D., Morgan D. and Yardley B. (2020) Light rare earth element redistribution during hydrothermal alteration at the Okorusu carbonatite complex, Namibia. *Mineraogical Magazine*, **84**, 49–64.

Chakhmouradian A.R. and Dahlgren S. (2021) Primary inclusions of burbankite in calcite carbonatites from the Fen carbonatite complex, southern Norway. *Mineralogy and Petrology*, **115**, 161–171 https://doi.org/10.1007/s00710-021-00736-0.

Chakhmouradian A.R., Reguir E.P. and Zaitsev A.N. (2016) Calcite and dolomite in intrusive carbonatites. I. Textural variations. *Mineralogy and Petrology*, **110**, 333–360.

Chakhmouradian A.R., Cooper M.A., Reguir E.P. and Moore M.A. (2017) Carbocernaite from the Bear Lodge carbonatite, Wyoming: revised structure, zoning and rare-earth fractionation on a microscale. *American Mineralogist*, **102**, 1340–1352.

Cooper A.F., Collin, A.K., Palin J.M. and Sprat, J. (2015) Mineralogical evolution and REE mobility during crystallisation of ancylite-bearing ferrocarbonatite, Haast River, New Zealand. *Lithos*, **216–217**, 324–337.

Dalsin M.I., Groat L.A., Creighton S. and Evams R.J. (2015) The mineralogy and geochemistry of the Wicheeda carbonatite complex, British Columbia, Canada. *Ore Geology Reviews*, **64**, 523–542.

Dawson J.B. (2008) *The Gregory Rift Valley and Neogene-Recent Volcanoes of Northern Tanzania*. Geological Society London, London.

Do Cabo V.N. (2014) *Geological, Mineralogical and Geochemical Characterization of the Heavy Rare Earth-Rich Carbonatites at Lofdal, Namibia*. PhD Thesis, Camborne School of Mines, University of Exeter, UK.

Do Cabo V.N., Wall F., Sitnikova M.A., Ellmies R., Henjes-Kunst F., Gerdes A. and Downes H. (2011) Mid and heavy REE in carbonatites at Lofdal, Namibia. Goldschmidt Conference Abstracts, Prague, *Mineralogical Magazine*, **75**, 770.

Dowman E., Wall F., Treloar P.J. and Rankin A.H. (2017) Rare-earth mobility as a result of multiple phases of fluid activity in fenite around the Chilwa Island Carbonatite, Malawi, *Mineralogical Magazine*, **81**, 1367–1395.

Effenberger H., Kluger F., Paulus H. and Wolfel E.R. (1985) Crystal structure refinement of burbankite. *Neues Jahrbuch für Mineralogie – Monatshefte*, **4**, 161–170.

Elliott H.A.I., Wall F., Chakhmouradian A.R., Siegfried P.R., Dahlgren S., Weatherley S., Finch A.A., Marks M.A.W., Dowman E. and Deady E. (2018) Fenites associated with carbonatite complexes: A review. *Ore Geology Reviews*, **93**, 38–59.

Estrada S., Henjes-Kunst F., Burgath K.P, Roland N.W., Schäfer F., Khain E.V. and Remizov D.N. (2012) Insights into the magmatic and geotectonic history of the Voikar Massiff, Polar Urals. *Zeitschrift der Deutschen Gesellschaft für Geowissenschaften*, **163**, 9–41.

Giebel R.J., Gauert C.D.K., Marks M.A.W., Costin G. and Markl G. (2017) Multi-stage formation of REE minerals in the Palabora Carbonatite Complex, South Africa. *American Mineralogist*, **102**, 1218–1233.

Gittins J. (1989) The origin and evolution of carbonatite magmas. Pp. 580–600 in: *Carbonatites: Genesis and Evolution* (K. Bell, editor). Chapman and Hall, London.

Graham S. and Keulen N. (2019) Nanoscale automated quantitative mineralogy: A 200-nm quantitative mineralogy assessment of fault gouge using Mineralogic. *Minerals*, **9**, 665.

Guzmics T., Mitchell R.H., Szabó C., Berkesi M., Milke R. and Abart R. (2011) Carbonatite melt inclusions in coexisting magnetite apatite and monticellite in Kerimasi calciocarbonatite Tanzania: melt evolution and petrogenesis. *Contribution to Mineralogy and Petrology*, **161**, 177–196.

Guzmics T., Zajacz Z., Mitchell R.H., Szabó C. and Wälle M. (2015) The role of liquid–liquid immiscibility and crystal fractionation in the genesis of carbonatite magmas: insights from Kerimasi melt inclusions. *Contribution to Mineralogy and Petrology*, **169**, 17.

Guzmics T., Berkesi M., Bodnar R.J., Fall A., Bali E., Milke R., Vetlényi E. and Szabó C. (2019) Natrocarbonatites: A hidden product of three-phase immiscibility. *Geology*, **47**, 527–530.

Halter W.E. and Webster J.D. (2004) The magmatic to hydrothermal transition and its bearing on ore-forming systems. *Chemical Geology*, **210**, 1–6.

Herman R.G., Bogdan C.E., Sommer A.J. and Simpson D.R. (1987) Discrimination among carbonate minerals by Raman spectroscopy using the laser microprobe. *Applied Spectroscopy*, **41**, 437–440.

Kapustin Yu.L. (1980) *Mineralogy of carbonatites*. Amerind Publishing, New Dehli, 259 pp.

Kapustin Yu.L. (1983) Features of fenitization around carbonatite bodies. *International Geological Reviews*, **25**, 1393–1404.

Keller J. (1989) Extrusive carbonatites and their significance. Pp. 70–88 in: *Carbonatites: Genesis and Evolution* (K. Bell, editor). Chapman and Hall, London.

Keller J. and Zaitsev A.N. (2006) Calciocarbonatite dykes at Oldoinyo Lengai, Tanzania: the fate of natrocarbonatite. *The Canadian Mineralogist*, **44**, 857–876.

Keller J. and Zaitsev A.N. (2012) Geochemistry and petrogenetic significance of natrocarbonatites at Oldoinyo Lengai Tanzania: composition of lavas from 1988 to 2007. *Lithos*, **152**, 47–55.

Keulen N., Malkki S.N. and Graham S. (2020) Automated quantitative mineralogy applied to metamorphic rocks. *Minerals*, **10**, https://doi.org/10.3390/min10010047

Le Bas M.J. (1989) Diversification of carbonatites. Pp.428–447 in: *Carbonatites: Genesis and Evolution* (K. Bell, editor). Chapman and Hall, London.

Le Bas M.J. (2008) Fenites associated with carbonatites. *The Canadian Mineralogist*, **46**, 915–932.

Migdisov A.A. and Williams-Jones A.E. (2008) A spectrophotometric study of Nd(III), Sm(III) and Er(III) complexation in sulfate-bearing solutions at elevated temperatures. *Geochimica et Cosmochimica Acta*, **72**, 5291–5303.

Migdisov A.A., Williams-Jones A.E. and Wagner T. (2009) An experimental study of the solubility and speciation of the rare earth elements (III) in fluoride- and chloride-bearing aqueous solutions at temperatures up to 300°C. *Geochimica et Cosmochimica Acta*, **73**, 7087–7109.

Migdisov A., Williams-Jones A.E., Brugger J. and Caporusci, F.A. (2016) Hydrothermal transport deposition, and fractionation of the REE: experimental data and thermodynamic calculations. *Chemical Geology*, **439**, 13–42.

Miller, R.M. (2008) Neoproterozoic and early Paleozoic rocks of the Damara Orogen. Pp. 13-1–114-1 in: *The Geology of Namibia*. (R.M. Miller, editor). Geological Survey Windhoek, Namibia.

Mills S.J., Kartashov P.M., Kampf A.R., Konev A.A., Koneva A.A. and Raudsepp M. (2012) Cordylite-(La), a new mineral species in fenite from the Biraya Fe–REE deposit, Irkutsk, Russia. *The Canadian Mineralogist*, **50**, 1281–1290.

Moore M., Chakhmouradian, A.R., Mariano A.N. and Sidhu R. (2015) Evolution of rare-earth mineralization in the Bear Lodge carbonatite, Wyoming: mineralogical and isotopic evidence. *Ore Geology Reviews*, **64**, 499–521.

Nadeau O., Cayer A., Pelletier M., Stevenson R. and Jébrak M. (2015) The Paleoproterozoic Montviel carbonatite-hosted REE–Nb deposit, Abitibi, Canada: Geology, mineralogy, geochemistry and genesis. *Ore Geology Reviews*, **67**, 314–335.

Namibia Rare Earths (2011, 2012, 2013, 2014) – Internal reports, and press releases from www.namibiarareearths.com.

Pekov I.V., Chukanov N.V. and Belovitskaya Yu. V. (1998) Khanneshite and petersenite-(Ce) from the Khibiny. *Zapiski Vserossiiskogo Mineralogicheskogo Obshchestva*, **127**, 92–100 [in Russian].

Schmidt R., Fitzek H., Nachtnebel M, Mayrhofer C., Schroettner H. and Zankel A. (2019). The combination of electron microscopy, Raman microscopy for the investigation of polymeric materials. *Macromolecular Symposia*, **384**, https://doi.org/10.1002/masy.201800237

Simmonetti A. and Bell K. (1995) Nd, Pb, and Sr isotope systematics of fluorite at Amba Dongar carbonatite complex, India; evidence for hydrothermal and crustal fluid mixing. *Economic Geology*, **90**, 2018–2027.

Subbotin V.V., Voloshin A.V., Pakhomovsky Ya.A. and Bakhchisaraitsev A.Yu. (1999) Calcioburbankite and burbankite from the Vuoriyarvi carbonatite massif (new data). *Zapiski Vserossiiskogo Mineralogicheskogo Obshchestva*, **128**, 78–87 [in Russian].

Swinden H.S. and Siegfried P. (2012) *43–101 Technical Report on the Rare Earth Element Occurrences in the Lofdal Carbonatite Complex, Kunene Region, Khorixas District, Namibia*. Published report for Namibia Rare Earths Ltd., Halifax, Canada.

https://doi.org/10.1180/mgm.2021.56 Published online by Cambridge University Press

Tuckler R.D., Belkin H.E., Schultz K.J., Peters S.G., Horton F., Buttlemann K. and Scott E.R. (2012) A major light rare-earth element (LREE) resource in the Khanneshin carbonatite complex, Southern Afghanistan. *Economic Geology*, **107**, 197–208.

Wall F. (2004) An illustration of the evolution and alteration of carbonatites using REE, Sr-rich carbonatites at Nkombwa, Zambia. Pp. 48–67 in: *Deep-seated Magmatism: Its Sources and their Relation to Plume Processes* (N. V. Vladykin, editor). Russian Academy of Sciences, Irkutsk – Ulan-Ude, Russia.

Wall F. and Mariano A.F (1996) Rare earth minerals in carbonatites: a discussion centred on the Kangankunde Carbonatite, Malawi. Pp. 193–225 in: *Rare Earth Minerals: Chemistry, Origin and Ore Deposits*. (A.P. Jones, F. Wall and C.T. Williams, editors) Mineralogical Society, London.

Wall F. and Zaitsev A.N. (2004) Rare earth minerals in Kola carbonatites. Pp. 341–373 in: *Phoscorites and Carbonatites from Mantle to Mine: The Key Example of the Kola Alkaline Province* (F. Wall and A.N. Zaitsev, editors). Mineralogical Society, London.

Wall F., Le Bas M.J., and Srivastava R.K. (1993) Calcite and carbocernaite exsolution and cotectic textures in a Sr, REE-rich carbonatite dyke from Rajasthan, India. *Mineralogical Magazine*, **57**, 495–513.

Wall F., Zaitsev A.N. and Mariano A.N. (2001) Rare earth pegmatites, *Journal of African Earth Sciences*, **32**, A35–A36.

Wall F., Niku-Paalova V.N., Storey C., Müller A. and Jeffries T. (2008). Xenotime-(Y) from carbonatite dykes at Lofdal, Namibia: unusually low LREE:HREE ratio in carbonatite, and the first dating of xenotime overgrowth on zircon. *The Canadian Mineralogist*, **46**, 861–877.

Wille G., Hollricher K. and Schmidt U. (2018) Exploring the unknown with correlative Raman imaging and scanning electron microscopy. *Spectroscopy*, **33**, 44–49.

Williams-Jones A.E., Migdisov A.A. and Samson I.M. (2012) Hydrothermal mobilization of the rare earth elements – a tale of 'ceria' and 'yttria'. *Elements*, **8**, 355–360.

Williams-Jones A.E., Wollenberg R. and Bodeving S. (2015) Hydrothermal fractionation of the rare earth elements and the genesis of the Lofdal REE deposit, Namibia. Pp. 125–130 in: *Symposium on Strategic and Critical Materials Proccedings* (Simandl G.J. and Neetz M., editors), British Columbia Geological Survey Paper, Canada.

Wooley A.R. and Kempe D.R.C. (1989) Carbonatites: nomenclature, average chemical composition, and element distribution. Pp. 1–14 in: *Carbonatites: Genesis and Evolution* (K. Bell, editor). Unwin Hyman, London.

Xu C., Taylor R.N., Kynicky J., Chakhmouradian A., Song W. and Wang L. (2011) The origin of enriched mantle beneath North China block: evidence from young carbonatites. *Lithos*, **127**, 1–9.

Yakovenchuk V.N., Ivanyuk G.Yu., Pakhomovsky Ya.A. and Menshikov Yu.P. (2005) *Khibiny*. (F. Wall, editor). Laplandia Minerals Ltd, Jyväskylä, Finland, 467 pp.

Zaitsev A.N. and Chakhmouradian A.R. (2002) Calcite–amphibole–clinopyroxene rock from the Afrikanda complex, Kola Peninsula, Russia: mineralogy and a possible link to carbonatites. II. Oxysalt minerals. *The Canadian Mineralogist*, **40**, 103–120.

Zaitsev A.N., Yakovenchuk V.N., Chao G.Y., Gault R.A., Subbotin V.V., Pakhomovsky Ya.A. and Bogdanova A.N. (1996) Kukharenkoite-(Ce), $Ba_2Ce(CO_3)_3F$, a new mineral from Kola peninsula, Russia and Quebec, Canada. *European Journal of Mineralogy*, **8**, 1327–1336.

Zaitsev A.N., Bell K., Wall F. and Le Bas M.J. (1997) Alkaline rare-earth element carbonates from carbonatites of the Khibina Massif: mineralogy and genesis. *Transaction (Doklady) of the Russian Academy of Sciences/Earth Science Sections Akademii Nauk*, **355**, 786–790.

Zaitsev A.N., Wall F. and Le Bas M.J. (1998) REE-Sr-Ba minerals from the Khibina carbonatites, Kola Peninsula, Russia: their mineralogy, paragenesis and evolution. *Mineralogical Magazine*, **62**, 225–250.

Zaitsev A.N., Demény A., Sindern S. and Wall F. (2002) Burbankite group minerals and their alteration in rare earth carbonatites – source of elements and fluids (evidence from C–O and Sr–Nd isotopic data). *Lithos*, **62**, 15–33.

Zaitsev A.N., Sitnikova, M.A., Subbotin V.V., Fernández-Suárez J. and Jeffries T.E. (2004) Sallanlatvi complex – a rare example of magnesite and siderite carbonatites. Pp. 201–245 in: *Phoscorites and Carbonatites from Mantle to Mine: The Key Example of the Kola Alkaline Province* (F. Wall and A.N. Zaitsev, editors). Mineralogical Society, London.

Zaitsev A.N., Wenzel T., Vennemann T. and Markl G. (2013) Tinderet volcano, Kenya: An altered natrocarbonatite locality? *Mineralogical Magazine*, **77**, 213–226.

Zdorik T.B. (1966) Burbankite and its alteration. *Trudy Mineralogicheskogo Muzeya. Akademii Nauk SSSR*, **17**, 60–75 [in Russian].

https://doi.org/10.1180/mgm.2021.56 Published online by Cambridge University Press